eng

MDPI

Article

Integrated Qualification Workflow for AISI 316 and 304L Stainless Steels Using Destructive and Eddy Current Non-Destructive Testing

Jude Emele [1], Ales Sliva [1], Mahalingam Nainaragaram Ramasamy [1,*], Silvie Brozova [2] and Ján Dižo [3]

[1] Faculty of Mechanical Engineering, VSB Technical University of Ostrava, 17. listopadu 15, 708 00 Ostrava-Poruba, Czech Republic
[2] Faculty of Materials Science and Technology, VSB Technical University of Ostrava, 17. listopadu 15, 708 00 Ostrava-Poruba, Czech Republic
[3] Faculty of Mechanical Engineering, University of Zilina, 17. Univerzitna 8215/1, 010 26 Zilina, Slovakia
* Correspondence: mahalingam.nainaragaram.ramasamy.st@vsb.cz

Abstract

This study establishes an integrated qualification workflow combining mechanical testing, microstructural characterization, and statistically defined eddy current testing (ECT) on the same material heats to provide a coherent and traceable material qualification methodology. Forged 316 and rolled 304L were fully annealed and subsequently subjected to a 700 °C/1 h low-temperature stress-relief (recovery) treatment. Room-temperature tensile testing and Charpy impact testing at room and cryogenic temperatures were performed alongside optical and electron microscopy to quantify grain size, δ-ferrite content, and representative fracture morphology under the investigated conditions. ECT responses were evaluated using a statistically defined threshold ($T = \mu + 3\sigma$) as a decision criterion for indication screening under assumed noise conditions and calibrated near-surface inspection sensitivity. The tested specimens showed stable measured mechanical responses, the examined fracture surfaces were consistent with predominantly ductile fracture behavior, and no reportable ECT indications were observed above the adopted threshold. The proposed framework provides a reproducible and scalable strategy for reducing uncertainty in material qualification and strengthening integration between destructive and non-destructive evaluation in stainless steel applications.

Keywords: austenitic stainless-steel qualification; destructive testing correlation; eddy current inspection; microstructure–property relationship; ECT-based indication screening

1. Introduction

Austenitic stainless steels AISI 316 and 304L are widely deployed in safety-critical components, yet property verification often proceeds along two separate tracks: destructive testing (DT) to establish strength/toughness and non-destructive testing (NDT) to screen for surface/subsurface discontinuities. Prior studies richly characterize mechanical behavior of 300-series stainless steels via tensile/Charpy testing [1] and separately demonstrate eddy current/test (EC/ECT) sensitivity to sensitization or near-surface defects [2,3]. However, integrated DT+NDT frameworks that (i) quantify microstructure (grain size, δ-ferrite), (ii) measure tensile and impact properties on the same heats, and (iii) support ECT-based screening for reportable surface and near-surface indications under production-relevant

Received: 31 March 2026
Revised: 11 May 2026
Accepted: 14 May 2026
Published: 18 May 2026

conditions for 316 and 304L, remain limited. Recent workflow-driven approaches emphasize integrating review, experimentation, and validation frameworks to avoid fragmented qualification decisions [4]. This separation hinders rapid, end-to-end validation needed by manufacturers [5,6].

This study addresses the gap using forged 316 and rolled 304L, both fully annealed and subsequently subjected to a low-temperature stress-relief (recovery) treatment at 700 °C for 1 h. We (i) quantify austenite grain size (LOM/ASTM E112) and δ-ferrite (ferrite meter); (ii) measure tensile and Charpy properties at room temperature (and Charpy at −196 °C); (iii) perform SEM fractography to identify failure mechanisms; and (iv) apply eddy current testing as an on-line-compatible NDT screen of the same materials. We ask the following: how do measured properties correlate with microstructure across processing routes, and what incremental value does ECT add to property qualification?

In contributions, we provide a coherent DT+NDT workflow for 316/304L that (i) links yield/UTS and Charpy response to measured grain size and δ-ferrite; (ii) shows representative fracture surfaces consistent with predominantly ductile fracture behavior at room temperature (RT); and (iii) demonstrates ECT-based screening for detectable surface and near-surface discontinuities alongside mechanical qualification. Practical relevance is emphasized by addressing ECT confounders (lift-off, conductivity, permeability) informed by electromagnetic fundamentals and material finish requirements [7–9]. The integrated evidence base is intended to shorten qualification cycles while maintaining traceable microstructure–property relationships for forged/rolled product forms [10,11].

Recent NDT approaches increasingly attempt to connect heat-treatment condition, material state, microstructure-sensitive physical properties, and mechanical behavior. Particularly, thermographic methods based on thermal diffusivity measurements have been proposed for assessing heat-treatment effectiveness and, in some cases, estimating mechanical-property trends in metallic materials [12–14]. Such approaches are valuable because thermal diffusivity may respond to changes in phase constitution, microstructure, residual stress state, and heat-treatment history. However, quantitative interpretation generally requires careful calibration, controlled thermal excitation, surface/emissivity control, coating consideration, specimen-thickness correction, thermal-boundary-condition management, and model-based fitting.

This work adopts a distinct qualification philosophy in which ECT is not used to predict yield strength, Charpy energy, ductility, grain size, or δ-ferrite content. Instead, tensile and Charpy testing define the mechanical response, while LOM/SEM characterize microstructure and fracture mode, and ECT provides a production-compatible screen for surface and near-surface discontinuities in the same material heats. This distinction is essential because ECT is applied here through calibrated inspection, skin-depth-limited coverage, lift-off control, and a $\mu + 3\sigma$ indication threshold, rather than as a mechanical-property prediction model.

The purpose of this study is grounded in the established relationships between microstructure and mechanical response in austenitic stainless steels. Specifically, it seeks to evaluate how variations in grain size and δ-ferrite content relate to yield strength and toughness through mechanisms such as dislocation interaction and solute redistribution. Eddy current testing is applied separately as a complementary integrity screening method to assess the absence of detectable near-surface discontinuities under controlled inspection conditions, without implying direct prediction of mechanical or microstructural properties.

2. Materials and Methods

2.1. Material Selection and Process

The process of extracting a small portion of material from a larger bulk sufficiently representative of the overall material and intended purpose is referred to as the bulk sampling method [15]. The original bulk diameters were approximately 369 mm for AISI 316 and 50 mm for AISI 304L; see Figure 1. After machining, final diameters of 341 mm and 45 mm, respectively, were obtained. These dimensional reductions are reported solely to ensure traceability between bulk material, specimen extraction, and subsequent testing. The percentage diameter reduction was calculated as

$$P(\%) = \frac{D_0 - D_f}{D_0} \times 100 \quad (1)$$

where D_0 is the initial diameter and D_f is the final diameter after machining. This calculation provides a simple measure of diameter reduction after machining and is used only to document dimensional traceability between the bulk material and extracted specimens. This formulation yields a positive value for material reduction [16].

Figure 1. Digitally measured bulk material diameters prior to machining and specimen extraction: A1—AISI 316 (D = 369 mm) and B1—AISI 304L (D = 50 mm). The figure documents the original section size and sampling provenance, ensuring dimensional traceability between bulk material, destructive testing specimens, and subsequent non-destructive evaluation.

After machining (turning/milling), the expected final delivery dimensions for the steel grades used in this study are 341 mm for AISI 316 and 45 mm for AISI 304L. These dimensions were also carefully and practically measured. The final delivery dimensions are presented in Section 3 of this study. The original bulk materials were fully annealed at 1040 °C for 1.5 h, followed by water quenching. Specimens measuring 20 mm × 20 mm were extracted from the mid-radius (½ radius) of the bulk materials along the longitudinal direction. These specimens were then heat-treated at 700 °C for 1 h, followed by air cooling, as a controlled low-temperature stress-relief (recovery) treatment.

The 700 °C/1 h exposure is interpreted as a low-temperature stress-relief (recovery) treatment in austenitic 304L/316, primarily promoting dislocation rearrangement and partial recovery. At this temperature, limited grain boundary carbide precipitation (e.g., M23C6) may occur according to literature-reported behavior for austenitic stainless

steels exposed within this temperature range [17,18], although the short exposure time is expected to restrict extensive sensitization. No obvious σ-phase features were identified in the microstructures examined; however, dedicated phase-identification techniques were not performed in the present study. The δ-ferrite fraction is not expected to change significantly under this treatment, as it is primarily determined during solidification, stable under subcritical heat-treatment conditions. These interpretations are consistent with established metallurgical behavior reported in the literature [10].

To differentiate between the two stainless steel (SS) grades used in this study, the sample labels and designations are presented in Table 1, while Table 2 presents the chemical compositions of the materials captured using a Niton XL2 X-ray fluorescence (XRF) spectrometer (Thermo Fisher, Waltham, MA, USA). Carbon was not quantified, as it cannot be reliably measured by handheld XRF, and is therefore not reported. A comparable XRF-based stainless steel characterization workflow using the Niton XL2 platform has been reported previously by Emele et al. [4].

Table 1. Sample labels and designations.

AISI 316	304L	Sample Condition
A1	B1	Fully annealed.
A2	B2	Stress-relieved at 700 °C for 1 h.

Table 2. Chemical compositions of the materials; wt.%.

Samples	Fe	Cu	Si	Mn	P	S	Cr	Ni	Mo
A1	balance	0.29	0.9	1.6	0.03	0.01	17.3	10.12	2.02
B1	balance	0.22	1.0	1.9	0.01	0.01	17.7	8.20	-

The microstructures of both stainless steel grades under varying conditions were examined using a scanning electron microscope (Zeiss Ultra 55 FEG-SEM, Oberkochen, Germany) and a light optical microscope (LOM, Leica DM4000 M, Wetzlar, Germany), each coupled to computer-based image analysis for quantitative evaluation. For metallographic preparation, specimens were mounted in epoxy, then ground and polished on a Tegramin-20 automatic system (Struers, Ballerup, Denmark). Etching was performed, as used in this study, a 1:1 mixture of 50 mL ethanol and 50 mL hydrochloric acid, to reveal grain boundaries and phase features. SEM analyses were conducted on the etched, resin-mounted samples and on the fractured surfaces of the tensile and Charpy V-notch specimens. Representative samples and the corresponding SEM loading/handling steps are shown in Figure 2.

Charpy V-notch impact tests were performed to evaluate the energy absorption capacity and fracture behavior of the two stainless steel grades under both room temperature (+20 °C) and cryogenic conditions (−196 °C). Three sets of V-notched specimens, each measuring 10 mm × 10 mm × 55 mm with a 45° notch angle, were prepared for every material condition (i.e., for A1, A2, B1, and B2). The impact tests were designed to compare absorbed impact energy and fracture morphology at room temperature (+20 °C) and cryogenic temperature (−196 °C) and to evaluate whether ductile fracture behavior was retained under the tested conditions.

For tensile testing, four dog-bone-shaped specimens were precisely machined with a gauge length of 75 mm and width of 10 mm. Each specimen had an initial diameter of 10 mm, parallel length of 75 mm, gauge length of 50 mm, and cross-sectional area of

78.5 mm^2. Tensile testing was performed under controlled loading conditions using a universal testing machine (Shimadzu/Hegewald & Peschk, Nossen, Germany).

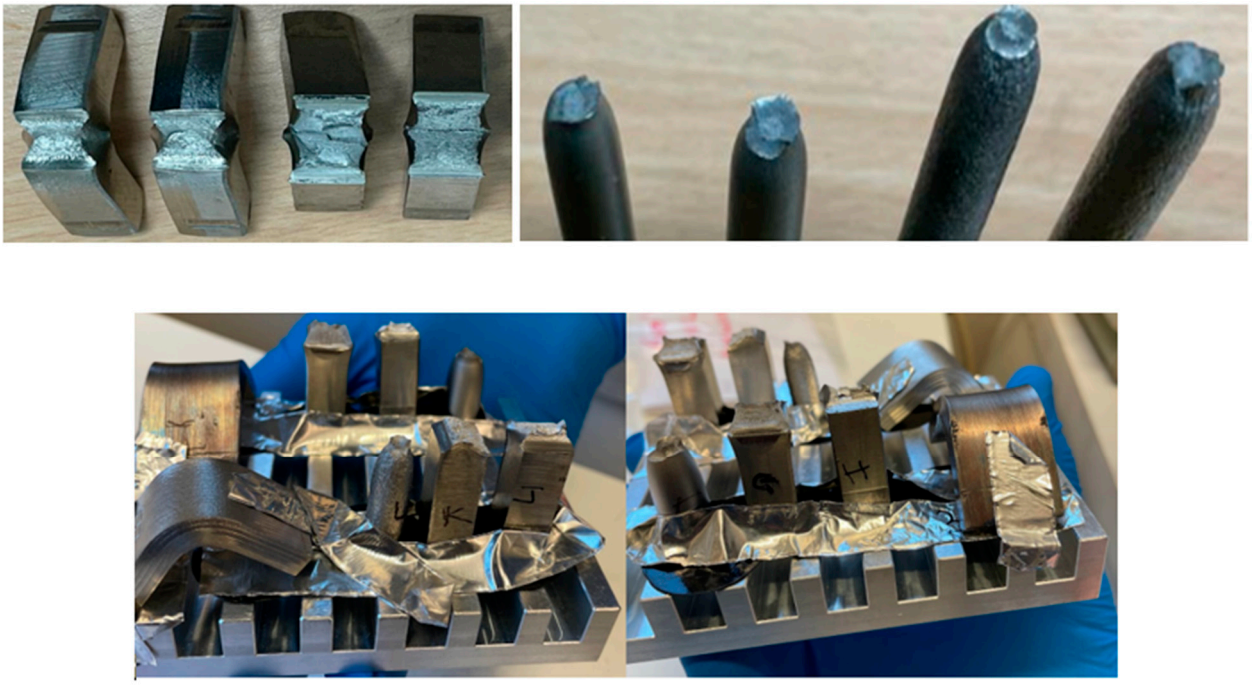

Figure 2. (**Top**) Cross sections of fractured Charpy V-notch specimens (A1, A2, B1, B2) and fractured tensile specimens (B2, B1, A2, A1). (**Bottom**) Representative broken specimens positioned for SEM loading. The figure establishes specimen-level traceability between mechanical testing and fractographic analysis within the integrated DT+NDT workflow.

2.2. Methodology

In this study, destructive testing (DT), including tensile and impact tests, was performed in conjunction with a non-destructive testing (NDT) method, specifically the eddy current technique (ECT), using state-of-the-art instrumentation. During testing, the applied load and corresponding elongation were continuously recorded to generate engineering stress–strain curves. From these data, the principal mechanical properties were determined using Equations (2)–(5).

$$\sigma = \frac{F}{A_0} \tag{2}$$

$$\sigma_y = \frac{F_{0.2}}{A_0} \tag{3}$$

$$\sigma_{UTS} = \frac{F_{max}}{A_0} \tag{4}$$

$$A = \frac{L_f - L_0}{L_0} \times 100 \tag{5}$$

where

σ (MPa) is the engineering stress;
σ_y (MPa) is the yield strength determined using the 0.2% offset method;
σ_{UTS} (MPa) is the ultimate tensile strength;
F (N) is the applied force;
$F_{0.2}$ (N) is the force at 0.2% offset yield;
F_{max} (N) is the maximum tensile force;
A_0 (mm^2) is the original cross-sectional area;
L_0 (mm) is the initial gauge length;

L_f (mm) is the final gauge length after fracture;
A (%) is the percentage elongation to failure.

However, the Charpy V-notch absorbed impact energy is reported in joules [19] and the associated uncertainty is documented for the tested specimens. Charpy impact energy is used here as an empirical measure of dynamic fracture resistance and should not be interpreted as a fracture-mechanics parameter such as K_{IC} or J_{IC}. Impact testing was conducted at both room temperature (+20 °C) and cryogenic temperature (−196 °C). SEM fractography (Zeiss Ultra 55 FEG-SEM, Oberkochen, Germany) was performed on one representative fractured specimen per condition (A1, A2, B1, and B2). The selected surfaces were consistent with the fracture features observed across the tested specimens and are considered representative of the overall fracture behavior. Light optical microscopy (LOM) was used to quantify microstructure and develop structure–property links. Moreover, LOM/SEM supported validation of the correlation between yield stress and grain size, commonly described by the Hall–Petch relation:

$$\sigma_y = \sigma_0 + \frac{k_y}{\sqrt{d}} \tag{6}$$

where

σ_y (MPa) is the yield strength;
σ_0 (MPa) is the lattice friction stress;
k_y (MPa·mm$^{1/2}$) is the Hall–Petch coefficient;
d (mm) is the average grain size.

Grain size d is expressed in mm in Equation (6); values measured in μm were converted accordingly.

The literature reviewed in this work was sourced from Google Scholar, Scopus, and Web of Science, focusing on destructive and non-destructive testing approaches for AISI 316 and 304L stainless steels. Based on this review, an integrated DT–ECT workflow was developed to ensure traceable qualification of mechanical properties and material integrity under production-relevant conditions.

Figure 3 summarizes the end-to-end validation process, beginning with representative bulk sampling, followed by heat treatment and specimen preparation. Destructive testing (tensile and Charpy impact) is first performed to establish baseline mechanical properties, after which microstructural characterization and fractographic analysis are used to identify the underlying deformation and fracture mechanisms. Eddy current testing (ECT) is then applied to the same material heats through calibration on reference standards and subsequent scanning under controlled conditions.

To reconcile differences between direct destructive measurements (force, extension, absorbed energy) and indirect non-destructive responses (impedance variation, lift-off sensitivity), an indirect parameter-control strategy was adopted. ECT was applied as a complementary screening method to assess whether reportable surface or near-surface indications were present above the adopted threshold under the defined inspection conditions. This correlation step provides a consistent interpretive framework despite the differing physical bases of DT and NDT measurements.

Both steels were assumed to have typical electromagnetic properties of austenitic stainless steels, namely low electrical conductivity on the order of ~10^5–10^6 S/m and near-unity relative permeability. These literature-based electromagnetic-property values were used solely for approximate engineering estimation of skin depth and were not experimentally measured for the investigated heats. Following ECT scanning, inspection results are evaluated using a statistically defined decision criterion, $T = \mu + 3\sigma$. If no

indication exceeds the threshold, the material proceeds within the qualification workflow. If an indication is detected, corrective actions such as rescanning, verification, or rework are initiated before re-evaluation. This closed-loop structure ensures that qualification decisions are both conservative and traceable, while avoiding unnecessary rejection of sound material.

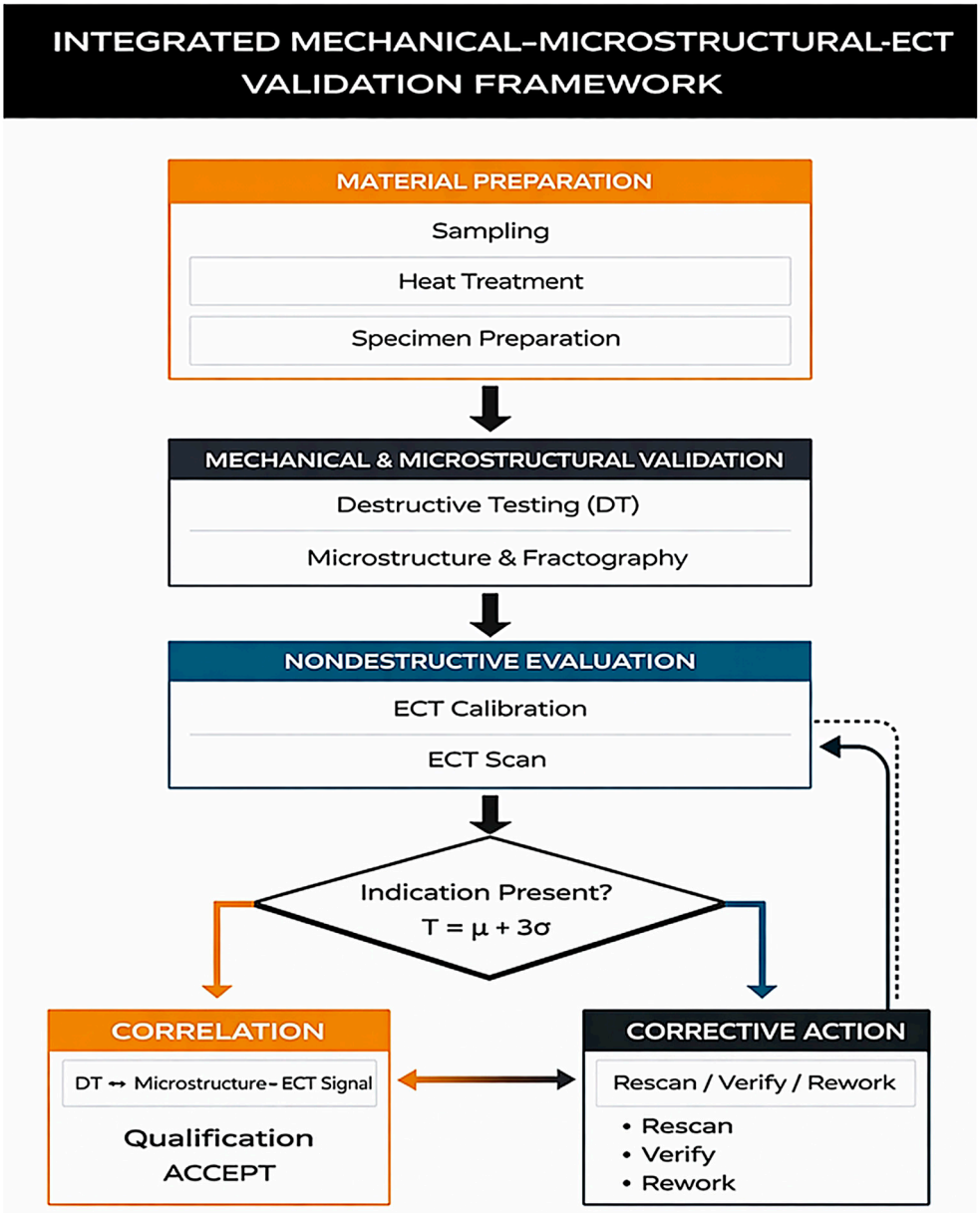

Figure 3. Integrated DT–ECT qualification workflow for AISI 316 and 304L stainless steels.

All schematic figures were developed by the authors using Python (Matplotlib) (version 3.11.4) and vector-based tools to ensure clear and reproducible representation of the workflow. The figures are simplified schematics intended to illustrate the testing sequence and process interactions relevant to the DT–ECT methodology.

2.3. ECT Acquisition and Decision Metrics

The 316 (Ø 341 mm) was scanned with a surface array coil and 304L (Ø 45 mm) with a ring/through-coil head under multi-frequency drive f = {50, 100, 200} kHz. Using literature-based approximate electromagnetic-property values typical of austenitic stainless steels ($\sigma \approx 1 \times 10^5$–$10^6$ S/m and $\mu r \approx 1$), the estimated skin depth, $\delta = \sqrt{[2\rho/(\omega\mu_0\mu r)]}$, was

within the millimeter range under the applied excitation frequencies. Using the assumed conductivity interval, the estimated skin depths were approximately

- $\delta \approx 7.1$–2.2 mm at 50 kHz;
- $\delta \approx 5.0$–1.6 mm at 100 kHz;
- $\delta \approx 3.6$–1.1 mm at 200 kHz, assuming $\mu r \approx 1$.

These values are approximate engineering estimates derived from literature-reported electromagnetic properties [20] and were not experimentally validated for the investigated heats. The estimated skin depths are intended only to demonstrate order-of-magnitude consistency between the selected excitation frequencies and the expected near-surface inspection regime.

Drive amplitude was fixed and lift-off held at 0.2 ± 0.1 mm using feelers/shims; the impact of lift-off and surface finish on EC response is well documented. Before each run, the instrument was nulled on a smooth reference and phase-rotated so lift-off lay on the x-axis of the impedance plane; artificial reflectors set amplitude scales, EDM slots $w = \{0.20, 0.43, 0.60\}$ mm, $L = \{0, 15, 25\}$ mm, and blind holes $D = \{0.3, 0.6\}$ mm, consistent with established EC calibration practice and prior probe studies [21].

All thresholding and acceptance criteria were applied independently for each probe configuration based on its respective calibration and noise statistics as different probe configurations were employed for AISI 316 (surface array) and 304L (through-coil), reflecting differences in geometry and inspection requirements. As a result, absolute eddy current signal amplitudes are not directly comparable between the two materials. Signal interpretation is therefore performed within each inspection configuration, and no cross-material amplitude comparison is implied without normalization through a common calibration procedure.

Lock-in demodulation produced in-phase X and quadrature Y (1 kHz low-pass), sampled at $\geq$10 kSa·s^{-1} per channel; spatial sampling used axial step $\leq 0.3 \cdot D_{coil}$ and track pitch $0.5 \cdot D_{coil}$ (~50% overlap). X and Y are the in-phase and quadrature components of probe impedance, respectively, and ΔZ represents the impedance variation relative to the baseline signal. Processing applied baseline removal, phase rotation, envelope detection, and C-scan maps:

$$\eta = \frac{|\Delta Z|}{\left|Z^0\right|} = \frac{|X + iY|}{\left|X^0 + iY^0\right|}$$

Noise statistics (μ_{noise}, σ_{noise}) were estimated on defect-free segments and the detection gate was set as $T = \mu + 3\sigma$, used here as a statistical thresholding criterion for indication screening. This formulation assumes approximately Gaussian noise, local stationarity of the signal baseline, and independence of decision windows; it controls the false-call probability but does not constitute a full Probability of Detection (POD) analysis. Accordingly, the $\mu + 3\sigma$ criterion is interpreted as a practical thresholding rule rather than a formal POD metric. The present methodology distinguishes between (i) threshold-based indication screening using $\mu + 3\sigma$, (ii) calibration-based detectability established using reference reflectors, and (iii) formal POD analysis, which was not performed in this study.

The $+3\sigma$ formulation assumes approximately Gaussian noise distribution; however, the noise distribution was not formally tested for normality in the present study and is therefore treated as an engineering approximation for threshold setting. Noise statistics were computed from defect-free regions after baseline removal and phase rotation. Independent decision windows were defined using spatial separation greater than one effective probe diameter to minimize autocorrelation. The normalized amplitude was calculated as $A_{norm} = |\Delta Z| / |Z_0|$. Table 3 summarizes the ECT noise statistics and decision thresholds

used to define the $\mu + 3\sigma$ decision rule. The reported values are representative of defect-free regions evaluated under calibrated inspection conditions.

Table 3. ECT Noise Statistics and Decision Thresholds.

Frequency (kHz)	μ_{noise} (A_{norm}, %)	σ_{noise} (A_{norm}, %)	Threshold $T = \mu + 3\sigma$ (%)	Independent Decision Windows (N)
50	0.012	0.0038	0.023	420
100	0.015	0.0042	0.028	395
200	0.018	0.0049	0.033	360

Amplitude-versus-size responses obtained from calibration standards were used to establish conservative detectability limits under the applied inspection conditions. However, no formal Probability of Detection (POD) analysis was performed [22], as this would require a controlled dataset of flawed specimens with known defect sizes and appropriate statistical modeling. Accordingly, the present results should be interpreted as calibration-based detectability bounds rather than POD-qualified detection capability. Both 316 and 304L satisfied the acceptance criteria across *f*, with lift-off-dominated loci and no defect arcs, consistent with the non-destructive results of Shen et al. [3] and Khedmatgozar Dolati [21].

Accordingly, the present ECT methodology should be interpreted as a calibrated screening approach for detectable surface and near-surface discontinuities under the applied inspection conditions, rather than as a comprehensive validation of overall material integrity or microstructural homogeneity.

2.4. Material Characterization

2.4.1. Mechanical Properties

Numerous testing models and experimental conditions have been developed to deepen the understanding of the mechanical behavior of stainless steel materials. These models and conditions play a crucial role in designing and manufacturing reliable and efficient stainless steel products. For example, the constitutive models for stainless steel at ambient temperatures have been proposed and applied to describe the ambient temperature behavior of stainless steel [23,24].

The mechanical response of the investigated steels is interpreted using established constitutive descriptions for austenitic stainless steels at ambient conditions, which capture the key features of smooth yielding and strain hardening. In the present study, the analysis is limited to experimentally obtained stress–strain behavior, and no predictive constitutive modeling is performed.

On the other hand, the Charpy V-notch impact testing method has become a standardized practice for material qualification [25–27]. It is particularly fundamental in stainless steel manufacturing for the classification of SS grades. The energy absorbed by Charpy V-notch specimens during testing is commonly used to determine a material's ductility or brittleness. For ductile materials, failure is typically associated with significant plastic deformation. Conversely, brittle fractures occur with little to no noticeable deformation and generally exhibit a flat fracture surface.

Under certain conditions, some materials may undergo a transition from ductile to brittle behavior, a phenomenon that can be readily observed through impact tests, particularly in body-centered cubic (BCC) transition metals [28]. The ductile-to-brittle transition in metals typically arises during high-speed machining operations, under low-temperature conditions, or in scenarios involving extremely high strain rates [29]. These transitional

effects and fracture characteristics can also be analyzed via the microstructures of the materials. For instance, Hwang et al. [28] investigated the influence of deformation-induced martensite and grain size on the ductile-to-brittle transition behavior of austenitic 18Cr–10Mn–(0.3~0.6)N stainless steel with varied alloying elements, using both Charpy impact tests and microstructural analysis. Microstructural analyses in the study [28] revealed that the austenite grain boundaries did not effectively inhibit brittle crack propagation, even though the trans-granular fracture units nearly matched the austenite grain size.

Consequently, both the Hall–Petch and Cottrell–Petch equations were modified by Hwang et al. [28] to better reflect the observed behavior. According to the modified equations, grain refinement plays a significant role in enhancing both yield and fracture stresses. The increase in stress is directly proportional to the Hall–Petch coefficient (k_y) and the Cottrell–Petch coefficient (k_f) respectively. In agreement with numerous other researchers, Hwang et al. [28] concluded that the yield stress of austenitic Cr–Mn–N stainless steels is influenced by three primary strengthening mechanisms: lattice friction strengthening, solid solution strengthening, and grain boundary strengthening. The modified Equations (7) and (8) proposed in Hwang et al.'s study are as follows:

$$\sigma_y = \sigma_i + \sigma_s + k_y d^{-½} \tag{7}$$

$$\sigma_f = k_f d^{-½} \approx \frac{4G\gamma_m}{k_y} d^{-½} \tag{8}$$

where

σ_y (MPa) represents yield stress;
σ_f (MPa) represents fracture stress;
σ_i (MPa) represents the lattice friction stress (often associated with the Peierls stress);
σ_s (MPa) represents solid solution strengthening;
k_y and k_f (MPa·mm^{½}) are material constants;
d (mm) stands for grain size;
G (MPa) stands for shear elastic modulus;
γ_m (J/m^2) represents effective surface energy.

To provide theoretical context for the mechanical response of stainless steels under varying thermal conditions, the relationship between temperature, yield stress, and fracture stress, together with the influence of grain size, is illustrated schematically in Figure 4 based on established literature models. The continuous and dashed curves represent coarse- and fine-grained microstructures, respectively. Grain refinement is generally associated with increases in both yield and fracture stresses and, in materials that exhibit a ductile-to-brittle transition, a shift in the transition to lower temperatures. While such behavior is well documented for BCC and some metastable systems, the present study does not attempt to determine a ductile-to-brittle transition temperature. Instead, the figure is included to provide general background on structure–property relationships relevant to low-temperature mechanical behavior.

However, certain parameters can influence the quality of measurements obtained during notch impact testing, and these are often expressed in terms of uncertainty values. In most cases, uncertainty is calculated from the test data, typically following standards such as ISO and ASTM [30,31]. The values of uncertainty should be carefully analyzed, and the influence of these calculations should be clearly understood [30]. Proper control and interpretation of these parameters are crucial in minimizing measurement uncertainty. Modern material testing techniques often allow for the simulation and experimental estimation of measurement uncertainties, providing values that closely match those required for accurate numerical predictions. While some advanced testing instruments are capable

of automatically computing uncertainty values, that functionality was not available in this study. Instead, pre-installed Excel-based equations were employed, including (a) the test piece's absorbed energy (J) manually input from the impact machine's analog reader; (b) the mean absorbed energy of 3 test pieces ($\overline{x}$); and (c) the standard uncertainty of mean absorbed energy.

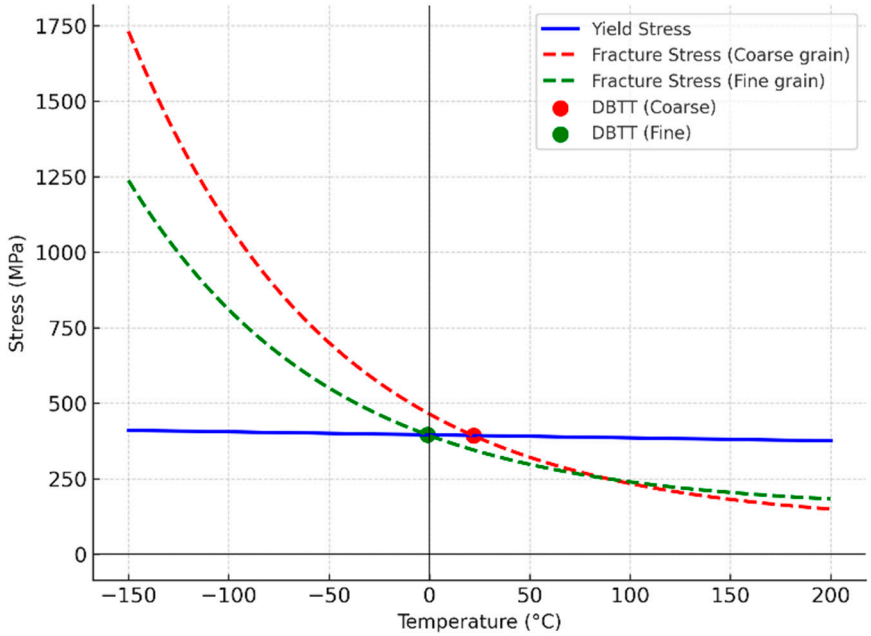

Figure 4. (Literature-based) schematic illustration of the influence of grain size on yield stress and absorbed energy in steels. The figure represents general trends reported in the literature and is not derived from the present experimental dataset.

For tensile testing, one specimen per condition was tested. The reported uncertainty values for tensile properties therefore represent measurement uncertainty associated with the testing system and data acquisition, rather than statistical variability. In contrast, Charpy impact results are reported as the mean of three specimens per condition, with uncertainty evaluated from the sample standard deviation.

Nevertheless, the equation for the standard uncertainty of mean absorbed energy is generally stated as follows:

$$u(\overline{x}) = \frac{s}{\sqrt{n}} \tag{9}$$

$$s = \sqrt{\frac{1}{n-1}\sum_{i=1}^{n}(x_i - \overline{x})^2} \tag{10}$$

where

$u(\overline{x})$ (J) is the standard uncertainty of the mean absorbed energy;
s (J) represents the standard deviation of the absorbed energy values;
x_i (J) is the absorbed energy of the i-th specimen;
$\overline{x}$ (J) represents the mean absorbed energy;
n is the number of tested samples.

The standard deviation (s) is influenced primarily by two factors [30]: the repeatability of the testing machine and the homogeneity of the specimen material. In this study, expanded uncertainties were calculated using a coverage factor k ≈ 2, corresponding to an approximate 95% confidence level, as recommended by Aydemir [30].

2.4.2. Eddy Current Testing

Eddy current testing is a non-destructive inspection technique widely applied for the detection of surface and near-surface discontinuities in metallic materials, including cracks, corrosion damage, and geometric irregularities [3]. By monitoring variations in probe impedance, information can be inferred regarding the presence, location, and characteristic size of material discontinuities [3]. The sensitivity and reliability of eddy current inspection are strongly influenced by probe design, excitation frequency, and signal processing strategies, all of which can be optimized to enhance defect detectability and spatial resolution.

Measured eddy current signals are influenced by multiple interacting factors, including probe lift-off, electrical conductivity, magnetic permeability, surface condition, and specimen geometry in austenitic stainless steels [3,20]. In this study, these effects were mitigated through controlled probe positioning, surface preparation, and calibration using reference standards prior to inspection.

Measurement setup and signal conditioning were adjusted to ensure stable coupling between the probe and the specimen surface, thereby minimizing lift-off-induced variability. Inspection sensitivity was governed by the electromagnetic skin depth, which defines the effective near-surface inspection volume and constrains detectability to surface and shallow subsurface regions. Within these physical limits, eddy current testing provided a robust integrity screening tool that complements destructive mechanical testing by supporting the absence of reportable surface-connected discontinuities in the inspected material heats.

3. Experimental Results and Analysis

3.1. The SEM Micrographs of the Forged AISI 316 Stainless Steel Grade

The SEM micrographs pertain to forged AISI 316 stainless steel that was fully annealed at 1040 °C for 1.5 h, water-quenched, and subsequently heat-treated at 700 °C for 1 h followed by air cooling. Figure 5 shows the as-received condition (A1) and the heat-treated condition (A2). Based on the SEM images, the average grain size of A1, measured by the linear-intercept method in accordance with ASTM E112-96 [32] was ~286 μm (SD = 10 μm). After the additional heat treatment, the average grain size of A2 increased slightly to ~292 μm (SD = 10 μm).

Micron-scale pores were observed in both A1 and A2 samples at magnifications exceeding 500×, with a higher density evident in the A1 specimen. These micro-pores did not show preferential localization along specific microstructural features, such as grain boundaries. Due to their presence, conventional optical microscopy failed to provide a clear delineation of grain boundaries. However, etching with aqua regia revealed more pronounced micro-pores in the A1 sample, but still enabled grain boundary visibility sufficient for SEM-based microstructural analysis.

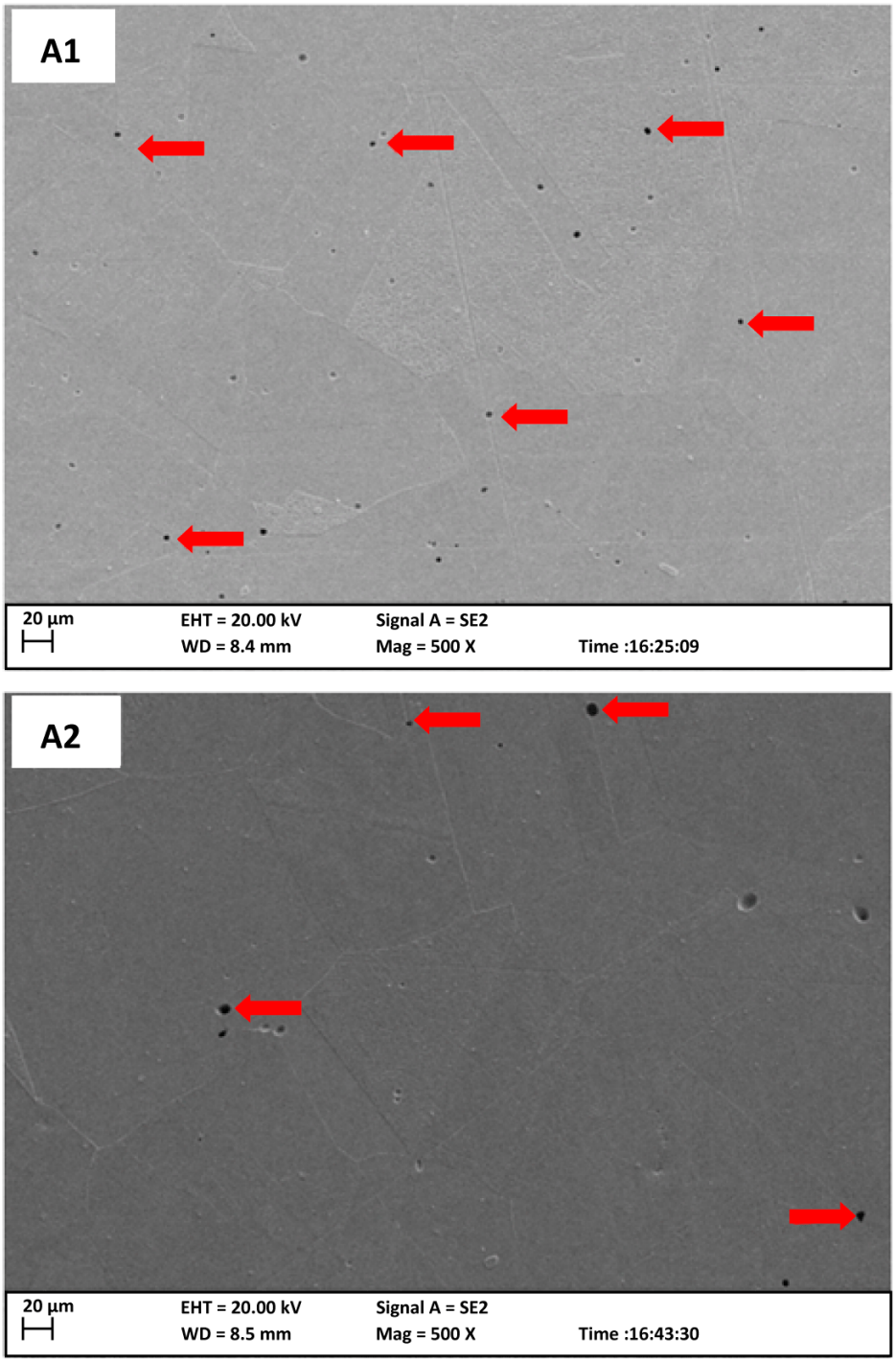

Figure 5. SEM micrographs of AISI 316 showing (A1) as received and (A2) after the 700 °C/1 h heat treatment (air-cooled). Specimens were polished and etched in aqua regia. Etching-induced micro-pits/void-like features indicated by few red arrows are visible on both conditions and should be interpreted as etch artifacts rather than intrinsic porosity.

3.2. The LOM Micrographs of the Forged AISI 316 Stainless Steel Grade

The microstructural features and corresponding grain-size histogram of the forged AISI 316 stainless steel, after full annealing at 1040 °C for 1.5 h followed by water quenching and subsequent heat treatment at 700 °C for 1 h with air cooling, are shown in Figures 6 and 7.

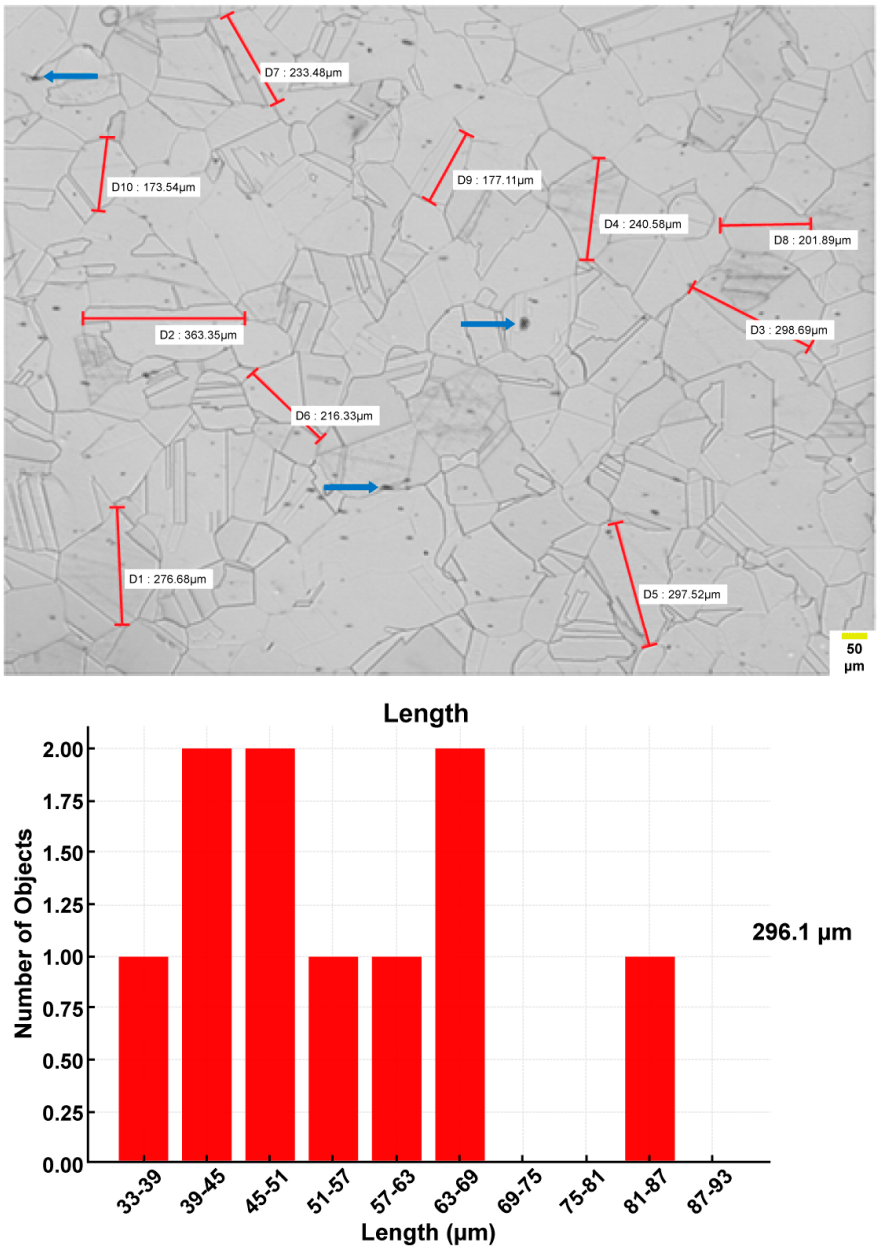

Figure 6. (**Top**) LOM micrograph of AISI 316 (A1), polished and etched with aqua regia (scale bar: 50 µm). Red rulers (D1–D10) denote representative linear-intercept chord lengths used for grain-size measurement; labels report individual chord values (µm). Blue arrows mark few etch pits/pull-outs produced during metallographic preparation, artifacts that were excluded from analysis and should not be interpreted as porosity. Grains appear polygonal/equiaxed, consistent with an annealed structure. (**Bottom**) Histogram of measured intercept lengths (red bars; y-axis = count). The mean grain size from the full dataset is 296.1 µm (noted at right).

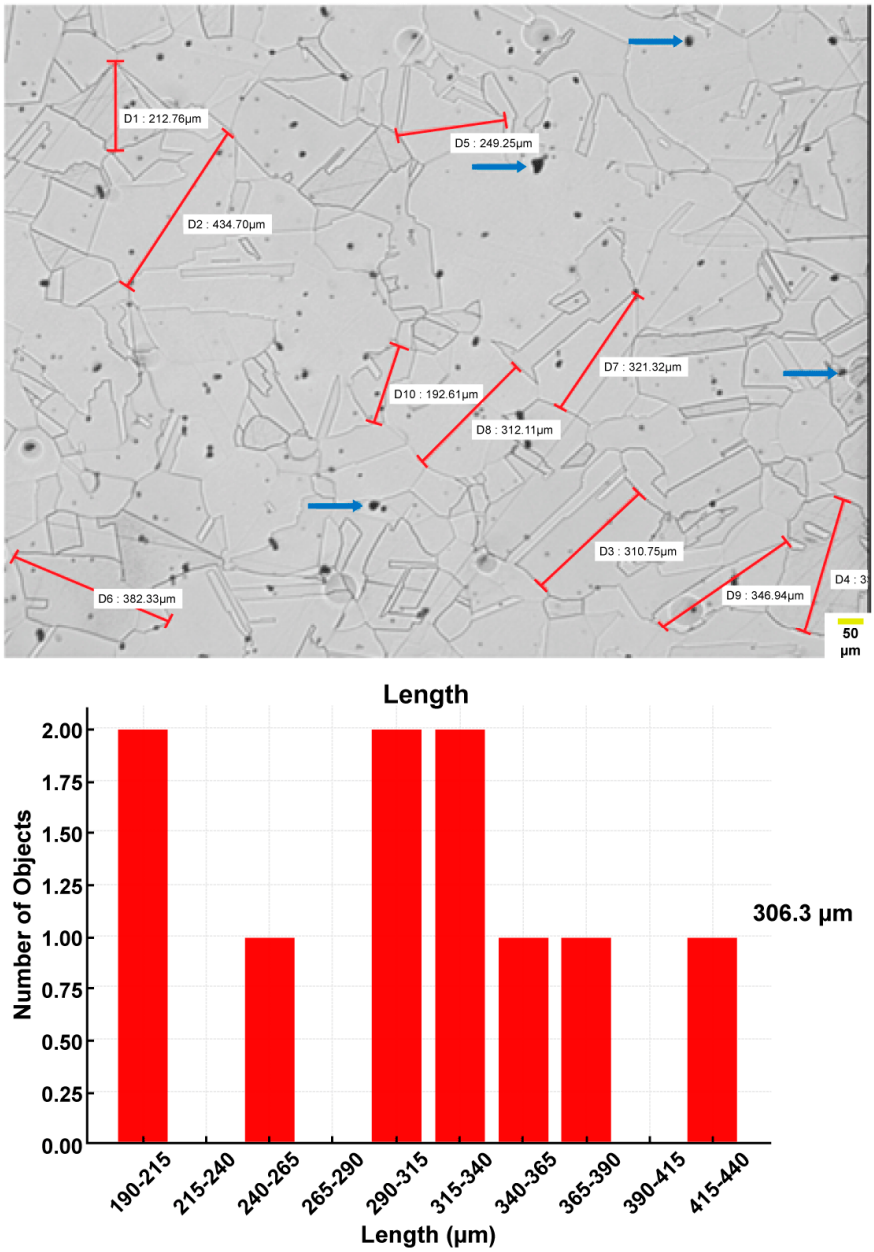

Figure 7. (**Top**) LOM micrograph of AISI 316 (A2: 700 °C/1 h, air-cooled), polished and etched with aqua regia (scale bar: 50 µm). Red rulers (D1–D10) show representative linear-intercept chord lengths used for grain-size measurement; labels report individual chord values (µm). Blue arrows mark preparation-induced etch pits/pull-outs, artifacts, not intrinsic porosity excluded from the analysis. Grains remain polygonal/equiaxed with slight coarsening relative to A1. (**Bottom**) Histogram of measured intercept lengths (red bars; y-axis = count). The mean grain size from the full dataset is 306.3 µm (noted at right).

3.3. The LOM Micrographs of the Rolled AISI 304L Stainless Steel Grade

The LOM microstructures and corresponding grain-size histogram of the rolled AISI 304L stainless steel, after full annealing at 1040 °C for 1.5 h followed by water quenching and subsequent heat treatment at 700 °C for 1 h with air cooling, are shown in Figures 8 and 9.

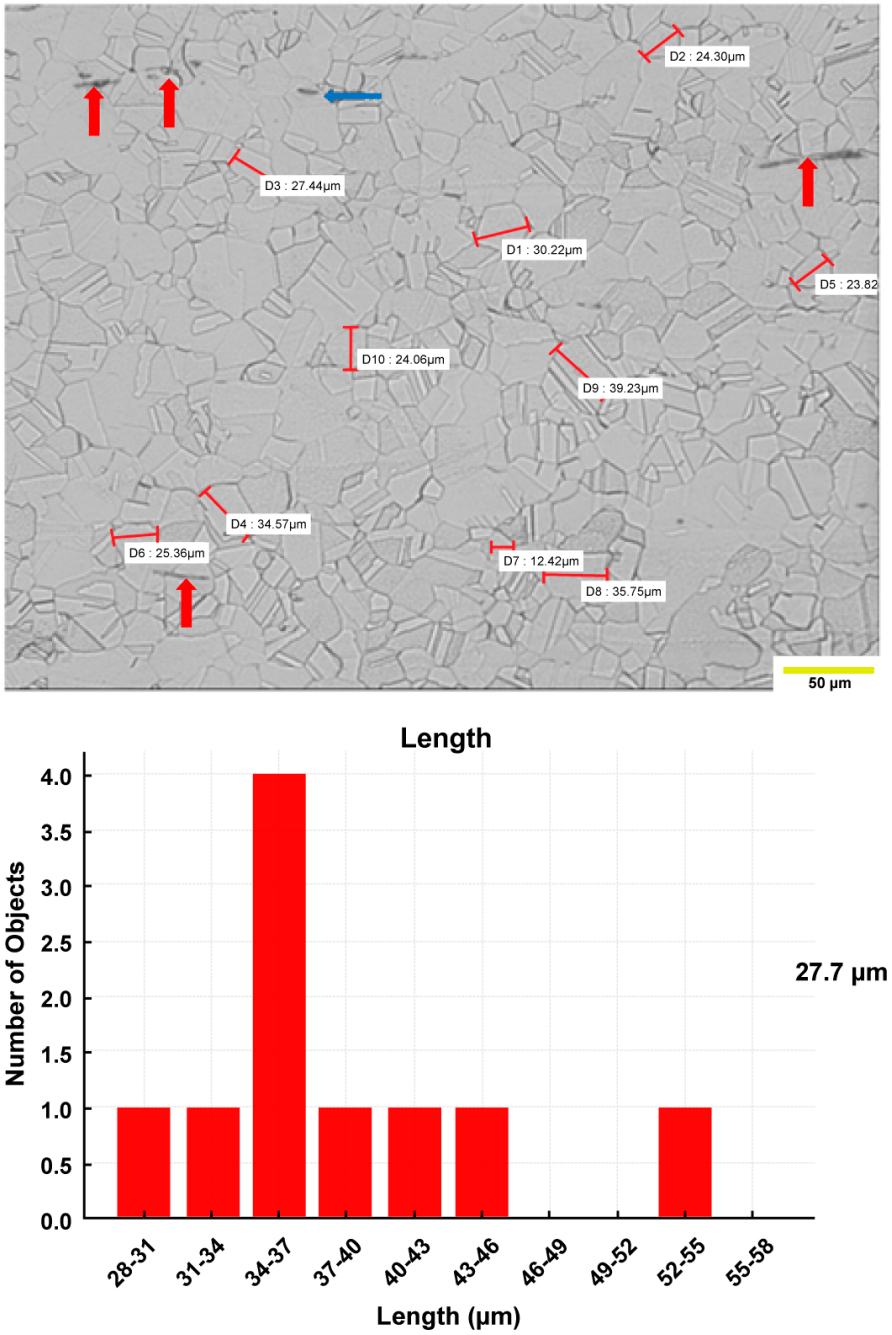

Figure 8. (**Top**) LOM micrograph of AISI 304L (B1, as received) polished and etched in aqua regia (scale bar: 50 µm). Red rulers (D1–D10) mark representative linear-intercept chords used for grain-size measurement; labels report individual lengths (µm). Red arrows indicate a small amount of δ-ferrite, visible as darker vermicular/stringer islands; these features were excluded from the austenite grain-size count (ferrite-meter value ≈ 1.8%). (**Bottom**) Histogram of measured intercept lengths (red bars; y-axis = count). The mean austenite grain size from the full dataset is 27.7 µm (noted at right).

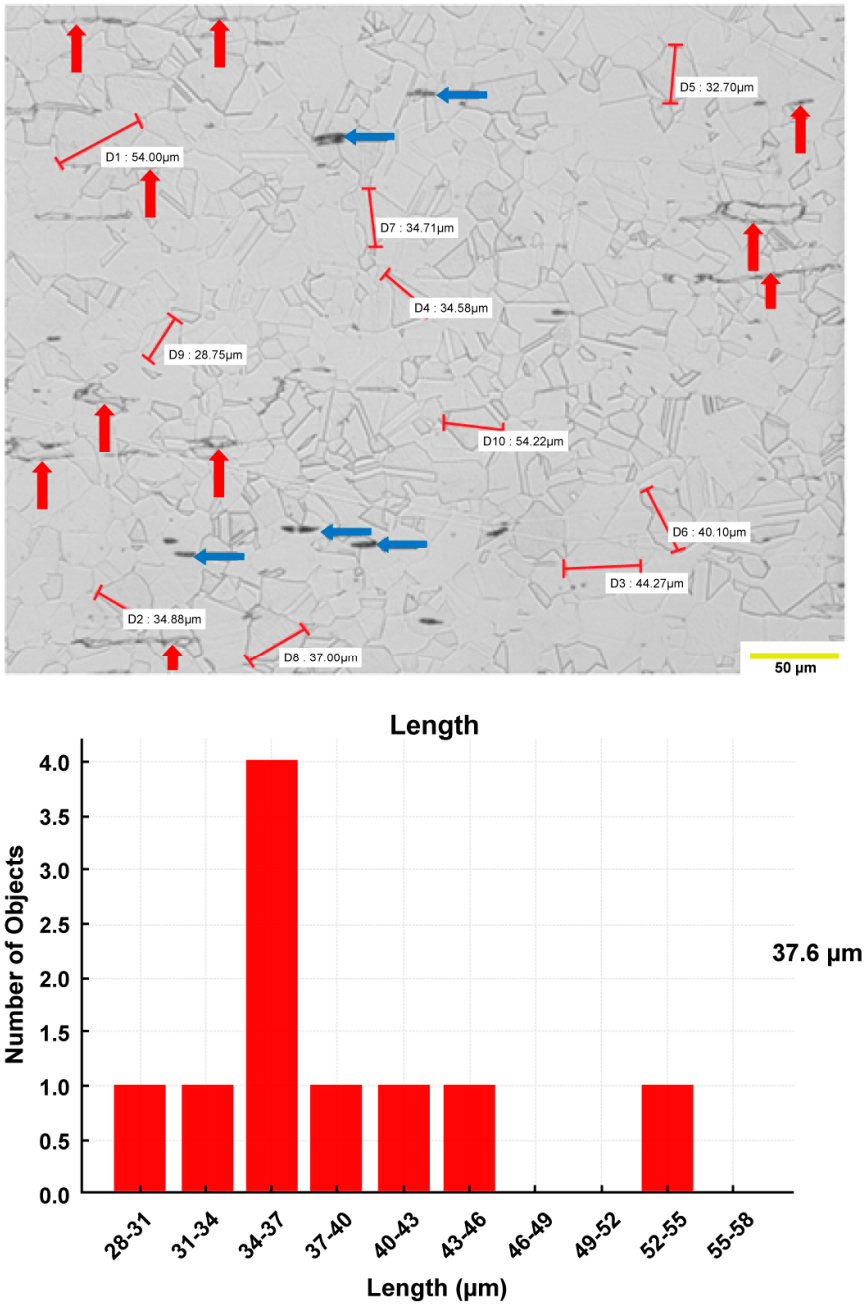

Figure 9. (**Top**) LOM micrograph of AISI 304L (B2, 700 °C/1 h, air-cooled) polished and etched in aqua regia (scale bar: 50 µm). Red rulers (D1–D10) mark representative linear-intercept chords used for grain-size measurement; labels give individual lengths (µm). Red arrows denote δ-ferrite islands/strings (≈3.0% by ferrite meter), which were excluded from the austenite grain-size statistics (blue arrows indicate minor polishing/etching streaks, artifacts). (**Bottom**) Histogram of measured intercept lengths (red bars; y-axis = count). The mean austenite grain size from the full dataset is 37.6 µm (noted at right).

3.4. The SEM Micrographs of the Tensile Specimens

Figure 10 presents the SEM images of fracture surfaces obtained from room temperature tensile-tested specimens for all investigated material conditions.

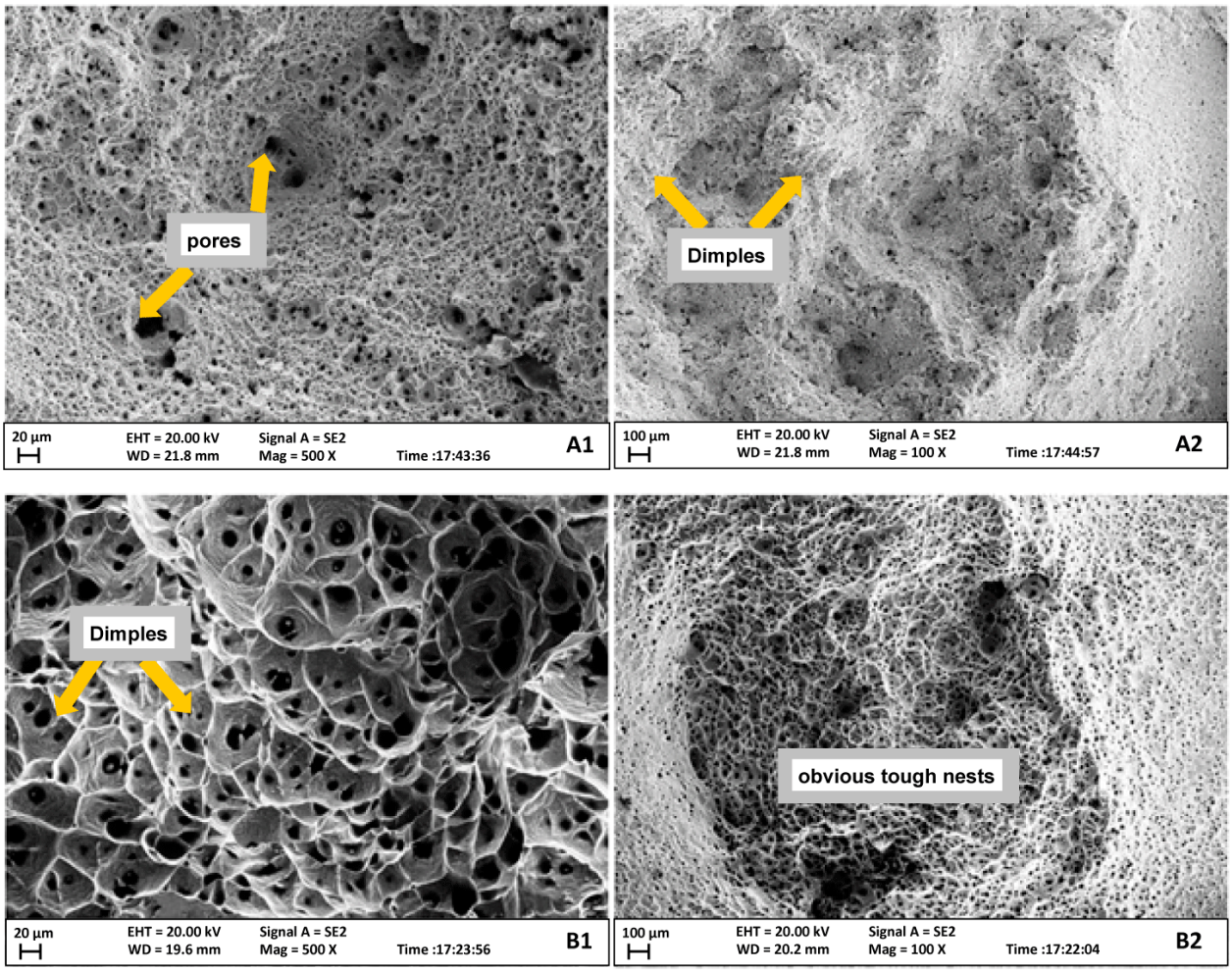

Figure 10. SEM fractography of tensile-tested specimens for AISI 316 (A1, A2) and AISI 304L (B1, B2), all tested at room temperature (+20 °C). The panels examined show ductile dimple rupture features characteristic of micro-void coalescence.

The examined panels show ductile damage features consistent with micro-void coalescence (MVC), involving void nucleation, growth, and coalescence, with peripheral shear-lip development and no evidence of cleavage or intergranular facets, generally consistent with austenitic steel behavior at room temperature. In 316, A1 (500×, 20 µm bar) shows dense fields of fine medium equiaxed dimples separated by thin ligaments. The yellow-arrowed pores mark discrete second-phase particles/voids at dimple bases that act as nucleation sites; the surrounding rounded tear ridges indicate stable void expansion prior to linking. A2 (100×, 100 µm bar) displays the same MVC mechanism; the coarser appearance arises largely from lower magnification and local necking rather than any change in fracture mode. Together, the 316 specimens exhibit consistent room temperature ductile fracture behavior characterized by micro-void coalescence.

The 304L surfaces also exhibit predominantly ductile features. B1 (500×) contains deep, uniformly equiaxed dimples with frequent particle-assisted nucleation, indicating substantial local plasticity consistent with the measured elongations. B2 (100×) develops a conspicuous "tough nest" zone, an intensely necked, fibrous web of ligaments in the fracture center, surrounded by fine peripheral dimples. Such tough nests form late in MVC when adjacent void sheets coalesce under elevated shear; they are a hallmark of stable ductile tearing and not suggestive of brittle crack advance.

Collectively, the examined representative fracture surfaces are consistent with predominantly ductile micro-void coalescence behavior under the investigated room-temperature

tensile conditions. Thus, the examined fracture surfaces do not suggest a clear fracture mechanism transition after the 700 °C treatment and more plausibly reflect subtle heat-treatment effects (e.g., solute redistribution and stabilized dislocation substructures) rather than grain-size control. The uniformly ductile morphologies in 304L also comport with its very low δ-ferrite fraction (≈1.8–3.0%), which lies well below the >10% regime associated with σ-phase-assisted embrittlement and loss of hot workability [33] further mitigating any tendency toward brittle fracture. Overall, the examined fracture morphologies are consistent with diffuse micro-void-coalescence-dominated tearing in both alloys under the investigated room-temperature tensile conditions.

3.5. The SEM Micrographs of the V-Notch Broken Specimens

Figure 11 is the SEM fractography labeled A1, A2, B1, and B2, providing detailed evidence of fracture mechanisms developed under Charpy impact loading. All images were captured at a magnification of 500×, with a 20 μm scale bar, enabling high-resolution interpretation of dynamic fracture morphologies.

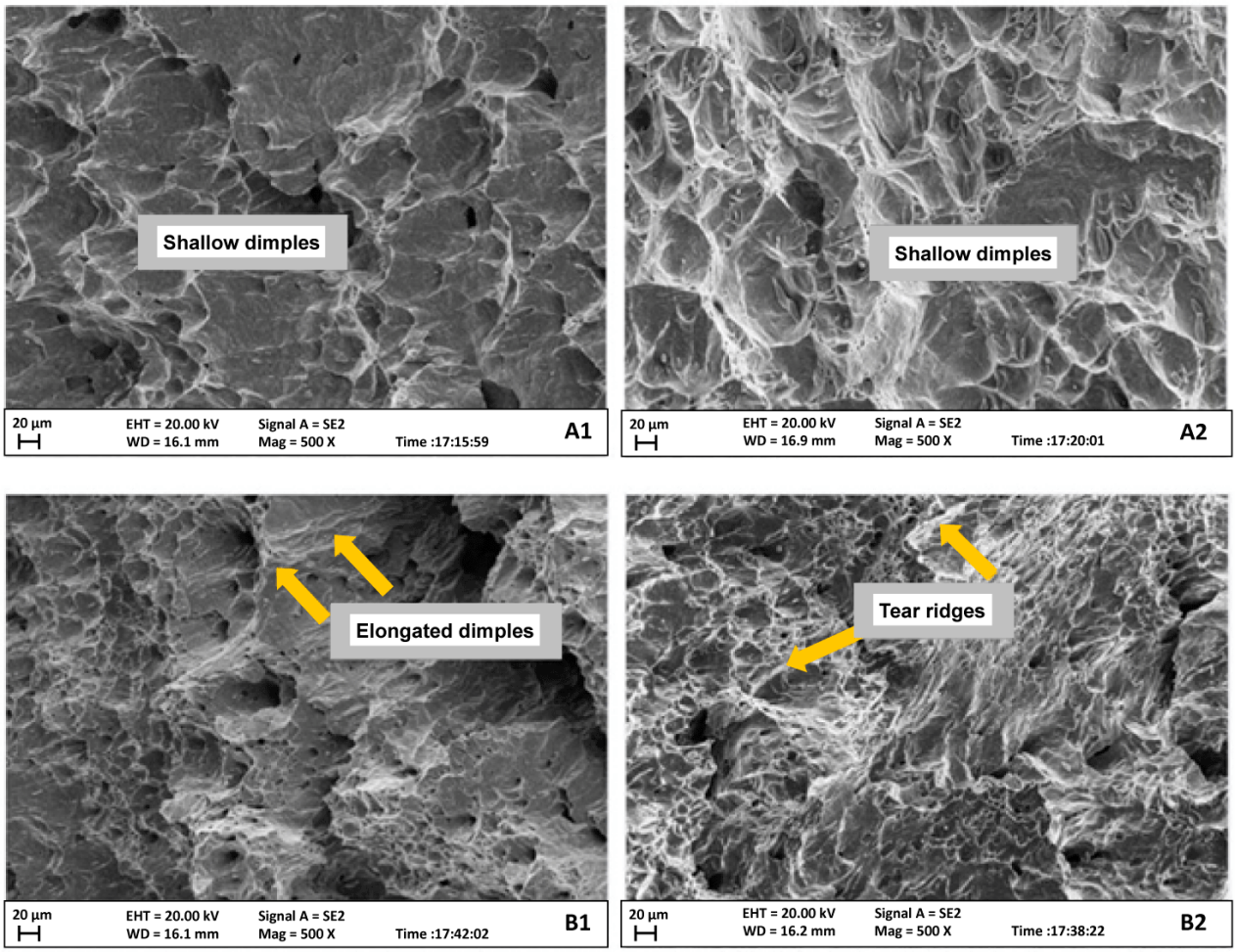

Figure 11. SEM images showing the impact fracture morphologies of all V-notch broken specimens: A1 (+20 °C), A2 (−196 °C), B1 (+20 °C), and B2 (−196 °C).

The examined A1–B2 fracture surfaces show features consistent with micro-void coalescence (MVC), involving void nucleation, growth, and coalescence, the hallmark of ductile failure in austenitic steels: equiaxed/elongated dimples bounded by ductile ligaments and intermittent tear ridges, with no river-patterned cleavage or intergranular facets [19]. In 316, both A1 and A2 (each at 500×, 20 μm bar) show shallow, uniformly distributed dimples (labels), indicating widespread inclusion-assisted void nucleation

followed by stable growth under high strain rate flow. The absence of faceting and the continuity of ligaments imply effective notch blunting and substantial plastic dissipation of impact energy, consistent with ductile Charpy responses reported for tough FCC alloys [26].

The 304L panels reveal stronger shear participation. B1 exhibits elongated dimples (yellow arrows), aligned with local maximum shear directions, typical of regions transitioning toward a peripheral shear lip. This morphology reflects a reduced triaxiality compared with the near-center zones, which promotes dimple stretching rather than equiaxing. B2 contains prominent tear ridges (yellow arrows) that segment dimple fields into vein-like patches; these ridges are classic ligamental instabilities that form late in MVC when adjacent void sheets link, again evidencing intense local plastic flow rather than brittle advance [19]. Notably, all images are collected at the same magnification, enabling direct comparison of dimple aspect ratios and ligament spacing relative to the 20 µm scale.

Taken together, the examined representative fracture surfaces suggest predominantly ductile damage evolution under the investigated impact conditions in both alloys. Differences among the examined panels, including equiaxed versus elongated dimples and the emergence of tear ridges, may be explained by spatial gradients in constraint and strain rate around the V-notch region, such as center versus shear-lip locations, rather than necessarily indicating a change in fracture mechanism. These MVC-dominated representative surfaces are consistent with high energy absorption and stable Charpy behavior observed experimentally, aligning with large-dataset trends for metallic structural materials [26] and canonical fracture-mechanism descriptions for steels [19].

3.6. Mechanical Properties Analysis

For tensile testing, one specimen per condition was tested. Because tensile testing was performed on a single specimen per condition, the reported tensile uncertainties should be interpreted as measurement uncertainty only. Replicate-based tensile variability was not assessed in this study. The mechanical response of the investigated steels is illustrated in Figure 12. The engineering stress–strain curves shown in Figure 12a are representative of the tensile behavior under the examined conditions. Markers denote experimentally measured data points extracted from tensile tests, while the associated error bars reflect the standard uncertainty at selected strain levels. The results indicate observable differences among the tested specimens; however, because tensile testing was performed on a single specimen per condition, these observations should not be interpreted as statistically validated material trends.

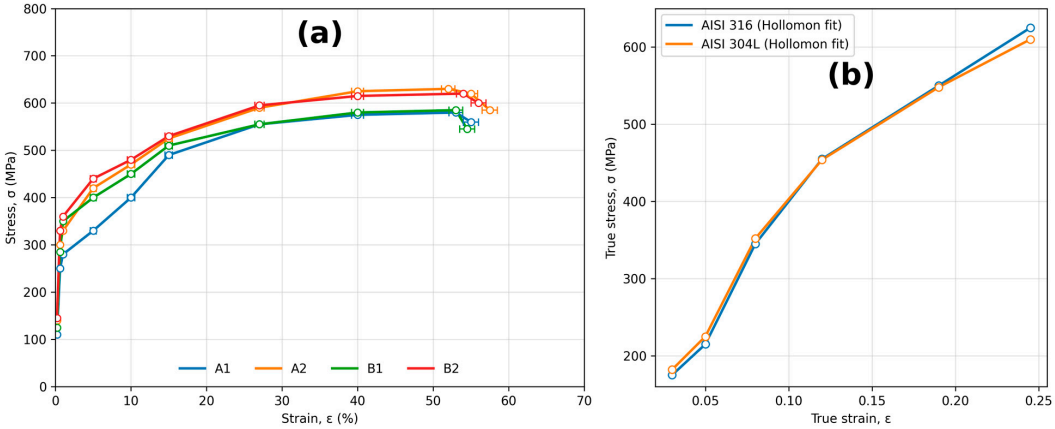

Figure 12. (**a**) Engineering stress–strain curves for AISI 316 and 304L steels. Markers denote experimental data; error bars indicate uncertainty (k = 2). Solid lines are guides to the eye. (**b**) True stress–strain curves with Hollomon fits in the uniform deformation region.

The corresponding true stress–strain relationships (Figure 12b) were derived from the engineering data and fitted using the Hollomon power law in the uniform deformation region, demonstrating good agreement with the experimental measurements.

Table 4 summarizes the key mechanical properties and microstructural characteristics of the analyzed AISI 316 and 304L stainless steel samples in both the as-received and heat-treated conditions. The table consolidates results from tensile testing, Charpy impact testing, and microstructural analysis, providing a concise comparison of strength, ductility, toughness, and grain size across processing routes and test temperatures.

Table 4. Summary of mechanical properties and microstructures of analyzed samples.

Characterization	A1	A2	B1	B2
Impact energy (J)	231 ± 9	200 ± 11	140 ± 13	143 ± 9
σ_y (MPa)	262 ± 1.8	306 ± 1.8	341 ± 1.7	361 ± 1.7
σUTS (MPa)	596 ± 0.9	636 ± 0.9	587 ± 0.8	619 ± 0.8
Elongation (A) %	56 ± 1.5	58 ± 1.5	55 ± 1.5	55 ± 1.5
Grain size—LOM, ($\bar{x}$) µm	296.1 ± 10	306.3 ± 10	27.7 ± 2	37.6 ± 3
Grain size—SEM, ($\bar{x}$) µm	~286 ± 1.0	~292 ± 1.0	–	–

Tensile uncertainties are based on single-specimen measurements and do not represent statistical material variability.

For the 304L grade, the yield strength (σ_y) ranged from 341 to 361 MPa, while the total elongation to failure (A) remained essentially constant at approximately 55% across all conditions. The elongation values were independently validated using Equation (5), with calculated results showing close agreement with the experimental measurements, consistent with recommended tensile property verification practices for steels [19]. The measured ultimate tensile strength values differed among the tested specimens: for the 316-grade samples, σUTS increased from 595 to 636 MPa, whereas the 304L-grade samples showed σUTS values between 587 and 619 MPa following the 700 °C heat treatment.

It is also noted that the uncertainties reported for all measured quantities are based on standard uncertainties multiplied by a coverage factor of k = 2, corresponding to an approximate confidence level of 95% for a normal distribution, in accordance with Aydemir [30]. The lowest average Charpy impact energy was recorded for sample B1, at approximately 140 J at room temperature. This value showed no significant change under cryogenic conditions (−196 °C), remaining at approximately 143 J. In contrast, the 316-grade samples exhibited a 13.4% reduction in absorbed energy at cryogenic temperature, decreasing from 231 J (A1) to 200 J (A2). Despite these differences, all fractured specimens displayed characteristics typical of ductile fracture, including pronounced necking and the formation of shear lips, as also shown in Figure 2. Compared with the 304L samples, the 316 specimens absorbed substantially more deformation energy under both test conditions, which is likewise evident from the macroscopic fracture appearance in Figure 2.

Microstructurally, the LOM-measured grain size of the forged AISI 316 samples increased by ≈3.45% following the applied heat treatment relative to the parent condition. When comparing the heat-treated forged 316 and rolled 304L materials, the grain-size percentage difference between samples A2 and B2 was ≈156.3%. SEM-based grain-size measurements for 304L were not performed; therefore, analysis relies on LOM-derived values, which are sufficient for comparative Hall–Petch assessment. However, SEM analysis of samples A1 and A2 indicated a slight increase in average grain size from ~286 µm to ~292 µm, corresponding to a ≈2.10% increase after heat treatment.

The rolled AISI 304L samples exhibited finer grain sizes than the forged AISI 316 grade and correspondingly higher yield strength (σ_y), a trend that is consistent with expectations from the Hall–Petch relationship [34]. As noted by Dunstan and Bushby [34], such behavior reflects size-dependent plasticity, wherein reduced microstructural length scales are associated with increased resistance to dislocation motion. Overall, differences in several measured mechanical properties were observed between the investigated conditions; however, replicate tensile testing would be required to establish statistically supported heat-treatment trends.

Because tensile testing was conducted on one specimen per condition, the tensile property comparisons presented here should be interpreted as exploratory observations rather than statistically validated population-level trends.

Hall–Petch Consistency Check

To gauge how much of the yield strength (σ_y) trends are attributable to grain size, the Hall–Petch relation (Equation (6)) is applied here as a qualitative consistency check, rather than as a basis for direct quantitative comparison between alloys:

$$\sigma_y = \sigma_0 + k_y d^{-½}$$

where d is the austenite grain size (mm), k_y is the Hall–Petch coefficient (MPa·mm^{½}) and σ_0 is the lattice/friction stress. Using the measured LOM grain sizes (Table 4) and the literature-consistent $k_y \approx 10$–32 MPa·mm^{½}, the grain-size contribution to changes in yield strength can be estimated as

$$\Delta\sigma_{HP} = k_y\left(d_2^{-½} - d_1^{-½}\right)$$

For AISI 316 (A1 → A2; 296.1 → 306.3 µm), $\Delta\sigma HP \approx -0.3$ to -1.0 MPa (negligible).

The observed increase in the measured yield strength for the tested specimen is unlikely to be explained solely by grain-size effects and may instead be qualitatively consistent with heat-treatment-related defect-structure evolution mechanisms, including solute redistribution and thermally stabilized dislocation configurations reported in the literature.

For AISI 304L (B1 → B2; 27.7 → 37.6 µm), $\Delta\sigma_{HP} \approx -8.5$ to -27 MPa (coarsening should reduce strength).

However, the tested specimen exhibited an approximately 20 MPa higher measured yield strength, indicating that heat-treatment-related effects in the tested specimen outweighed the small negative Hall–Petch contribution.

For the cross-alloy comparison at room temperature (A1–316: 296.1 µm vs. B1–304L: 27.7 µm), the estimated Hall–Petch increment is $\Delta\sigma_{HP} \approx +42$ to $+133$ MPa, while the measured σ_y difference is 79 MPa (341–262 MPa). This is broadly consistent with, but not solely determined by, grain-size strengthening.

However, this cross-alloy comparison must be interpreted with caution, as it is influenced by multiple confounding factors, including differences in alloy chemistry (e.g., Mo content), processing route (forged vs. rolled), crystallographic texture, and δ-ferrite fraction. Therefore, the observed strength differences cannot be attributed exclusively to grain size.

Overall, the Hall–Petch analysis indicates

(i) A negligible grain-size effect for 316 (A1 → A2);
(ii) A small negative grain-size contribution for 304L (B1 → B2) that is outweighed by other heat-treatment-related effects in the tested specimen;
(iii) A positive grain-size contribution for the room-temperature comparison of 304L vs. 316, consistent with finer grains contributing to higher strength, alongside composition and processing effects.

Thus, the observed strength differences between the as-received and heat-treated conditions are interpreted primarily in terms of defect-structure evolution and heat-treatment effects rather than grain-size changes.

3.7. Eddy Current Testing Results

Eddy Current Testing (NDT): Quantitative Results

Figure 13 shows AISI 316 (341 mm) and 304L (45 mm) bars with smooth and uniform machined surfaces, allowing stable probe coupling and continuous longitudinal scanning during testing while minimizing lift-off variation and maintaining consistent impedance-response conditions.

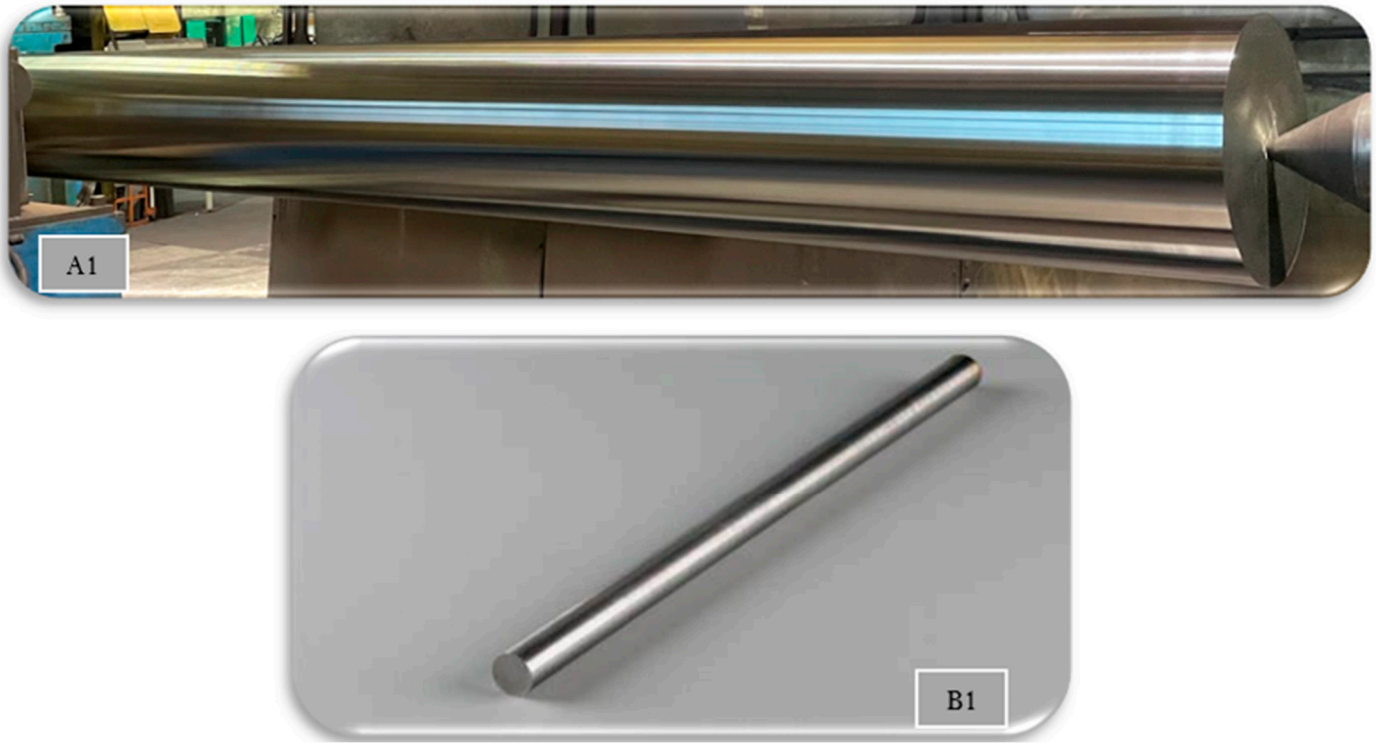

Figure 13. Representative eddy current testing (ECT) response of the examined (A1) AISI 316 and (B1) 304L specimens after calibration and lift-off control. The absence of reportable indications above the adopted threshold indicates that no detectable surface or near-surface discontinuities exceeding the calibrated inspection sensitivity were observed under the applied inspection conditions.

Prior to ECT, the bars were machined to match engineering-defined dimensions: AISI 316 from 369 → 341 mm (7.59% diameter reduction) and 304L from 50 → 45 mm (10.0% reduction), computed using P (%) = 100 (B−F)/B with $B > 0$. (Equation (1)). These reductions ensured full probe access and consistent surface finish, critical for reliable EC response [3,35]. ECT was performed on the same heats using (i) an array coil for the 316 bar and (ii) a through-coil ring probe for the 304L bar, enabling circumferential coverage with axial scanning. Areal coverage was essentially complete; $C = A_{scanned}/A_{total} \approx 1.00$. Frequency selection and coil geometry were guided by approximate skin-depth estimates derived from the literature-reported electromagnetic-property ranges for austenitic stainless steels [3,21].

Target detectability was set so intended flaw depths were $O(\delta)$ (surface/near-surface sensitivity), consistent with line inspection practice. Signal discrimination used a noise-referenced threshold on the impedance plane: if X denotes the demodulated amplitude, the decision threshold was $T = \mu_b + k\,\sigma_b$, $k = 3$, where μ_b, σ_b are the baseline mean and standard deviation from defect-free regions. Under an approximate Gaussian noise as-

sumption, the $\mu + 3\sigma$ threshold corresponds to a theoretical one-sided false-call probability of approximately 0.13% per independent decision; however, the noise distribution was not formally tested for normality in the present study, and this value should therefore be interpreted only as an engineering approximation rather than a validated statistical reliability metric. Under these conditions, the binomial 'rule of three' provides only an approximate statistical upper bound under the assumptions of independent decision windows and threshold-based indication screening and should not be interpreted as a formal POD-qualified detection reliability metric. This bound reflects the absence of observed indications under the tested conditions and should not be interpreted as a formal Probability of Detection (POD) estimate.

Detectability values reported in simulation-informed studies, such as the ANSYS-based work of Farag et al. [35], are useful for contextual comparison but are not directly transferable to the present experiment because they depend strongly on probe geometry, material properties, specimen geometry, lift-off, excitation frequency, and calibration conditions. Therefore, the present ECT results are interpreted only within the applied inspection configuration and calibration procedure.

Within these conditions, no reportable indications were observed above the adopted threshold. This result indicates that no detectable surface or near-surface discontinuities exceeding the calibrated inspection response were identified in the scanned regions. The outcome is consistent with the smooth machined surface, the near-unity relative permeability of the austenitic matrix, and the low δ-ferrite fraction in 304L, which reduces magnetic heterogeneity that could complicate EC signal interpretation [36].

Overall, the ECT program provides (a) near-complete geometric coverage, (b) a noise-referenced thresholding criterion $T = \mu_b + 3\sigma_b$ for indication screening, and (c) calibration-based screening for detectable surface and near-surface discontinuities under the applied inspection conditions. These results complement the destructive testing program by reducing the likelihood that detectable near-surface discontinuities influenced the measured mechanical response, but they do not constitute direct mechanical-property validation, simulation-transferable flaw sizing, or a formal POD assessment. The present ECT methodology therefore provides practical threshold-based indication screening and calibration-referenced detectability assessment under the applied inspection conditions, but it does not constitute a formal POD-qualified inspection reliability analysis.

4. Discussion

This discussion interprets the relationships between microstructural features, fracture morphologies, and bulk mechanical behavior to elucidate the underlying structure–property interactions within the proposed integrated qualification workflow. The analysis provides a physically grounded basis for explaining the observed trends and demonstrates the consistency of the combined destructive testing (DT) and eddy current testing (ECT) approach.

4.1. Mechanical Properties: Experimentally Obtained Engineering Stress–Strain Curves

The engineering stress–strain curves exhibit smooth, continuous hardening up to uniform elongation, characteristic of austenitic steels governed by dislocation-mediated plasticity. The flow behavior was analyzed in the context of constitutive models proposed by Rasmussen [24] and extended by He et al. [23]. In the uniform deformation region, the true stress–strain response is well approximated by the Hollomon relationship, $\sigma = K\,\varepsilon^n$, as shown in Figure 12b. Fitting yielded $n \approx 0.48$–0.52 and $K \approx 1.2$–1.3 GPa for both 316 and 304L, consistent with reported values for annealed austenitic stainless steels.

For the tested specimens, the post-treatment stress–strain curves exhibited slightly higher measured yield stress values, implying that the observed differences may be associated with thermally stabilized defect structures and solute redistribution, although the present tensile dataset is insufficient to establish statistically validated causality. According to He et al. [23], such behavior corresponds to a vertical shift in the stress–strain curve with minimal change in curvature, characteristic of thermally stabilized substructures.

Overall, the experimental response is qualitatively consistent with the constitutive descriptions reported by Rasmussen [24] and He et al. [23] for austenitic steels at low strain rates, including smooth yielding and sustained work hardening. The apparent limited variation in the fitted strain hardening exponent, n, should be interpreted cautiously because tensile testing was performed on a limited number of specimens. These observations support the use of combined mechanical testing and structured validation frameworks to improve traceability from processing to material response, consistent with recent studies on stainless steel qualification [4].

4.2. Toughness, Fracture Mode, and Cryogenic Behavior

A key outcome is the retention of ductile fracture behavior in both grades at −196 °C under the tested conditions. Charpy energy in 316 decreases moderately (231 → 200 J), while 304L is essentially unchanged (~140 → 143 J within combined uncertainty); in all cases, the fracture surfaces show dimples and shear lips, i.e., ductile failure at both room and cryogenic temperatures, as shown in Figures 10 and 11. This is consistent with FCC austenitic behavior, which maintains toughness at low temperature because of multiple operative slip systems and the lack of a true cleavage plane as reported in the literature.

The measured δ-ferrite in 304L (~1.8–3.0%) is well below the >10% threshold associated with embrittlement and σ-phase-assisted degradation reported by Arata et al. [33]. No obvious σ-phase features were identified in the SEM observations performed in the present study, although dedicated phase-identification methods were not applied. This aligns with reports in the literature that small δ-ferrite contents (<~5%) can improve solidification crack resistance without sacrificing low-temperature toughness.

Although strain-induced martensitic transformation can occur in metastable austenitic stainless steels under cryogenic deformation, the stable Charpy energy and fully ductile fracture morphologies observed here indicate that any such transformation was insufficient to induce a ductile-to-brittle transition (DBT). In contrast, ferritic stainless steels with BCC crystal structures exhibit a pronounced DBT, characterized by sharp reductions in absorbed energy and cleavage-dominated fracture as temperature decreases [37,38].

The retained low-temperature toughness of both 316 and 304L in the present study is qualitatively consistent with the stability of the austenitic FCC matrix, the low δ-ferrite content, and continued strain hardening under cryogenic conditions, in agreement with established ductile fracture behavior in austenitic steels [19] and ferrite-related embrittlement considerations reported in the literature [33,39,40]. The observed differences in measured tensile strength are qualitatively consistent with heat-treatment-related microstructural and defect-structure effects rather than grain-size effects alone, in agreement with the Hall–Petch analysis discussed separately [34].

4.3. Position of the DT–ECT Workflow Relative to Thermographic NDT Methods

Thermographic NDT methods provide a useful comparison because pulse photothermal and photothermal-radiometry approaches can reconstruct thermal effusivity or diffusivity profiles that are sensitive to depth-dependent material state, heat-treatment condition, crystallographic texture, hardness, and mechanical-behavior trends [12–14]. However, these methods generally require controlled thermal excitation, surface/emissivity man-

agement, specimen-thickness and heat-loss considerations, and inversion or model-based interpretation [12–14].

In contrast, the ECT component of the present workflow is used as a rapid, production-compatible integrity screen for surface and near-surface discontinuities; it does not require thermal excitation or thermal diffusivity fitting, but remains sensitive to lift-off, surface condition, probe configuration, and calibration transferability. The present ECT workflow also does not provide direct mechanical-property prediction and does not include formal Probability of Detection (POD) validation, as no controlled flawed specimen dataset was used. Accordingly, ECT is treated here as a complementary defect screening step, while mechanical and microstructural properties are established by destructive testing and metallographic characterization.

5. Conclusions

This study presents an integrated, production-relevant qualification workflow for AISI 316 and 304L austenitic stainless steels by combining destructive testing, eddy current testing (ECT), and quantitative microstructural characterization on the same material heats. The approach enables a consistent and traceable assessment of relationships between microstructure, mechanical performance, and electromagnetic inspection response, thereby reducing fragmentation in conventional validation workflows.

Both alloys exhibited stable mechanical performance, characterized by smooth work hardening, high ductility ($A \approx 55$–58%), and consistent strength levels (σ_y = 262–361 MPa; σUTS = 587–636 MPa). Charpy testing showed retained cryogenic impact resistance at -196 °C, with ductile fracture features observed under the tested conditions. The SEM fracture surfaces examined were consistently characterized by ductile micro-void-coalescence-type morphologies under the investigated conditions. Eddy current testing (ECT), applied under controlled conditions using a $\mu + 3\sigma$ threshold criterion, identified no reportable indications. This result indicates that no surface or near-surface discontinuities exceeding the calibrated detection limits (~0.3–0.6 mm, based on reference standards) were detected under the applied inspection conditions. These ECT results should be interpreted within the limits of the applied inspection configuration, calibrated sensitivity range, and near-surface detection capability, and do not exclude all possible defects or metallurgical heterogeneity.

Microstructural analysis showed coarse-grained AISI 316 (~300 μm) and fine-grained AISI 304L (~28–38 μm), with low δ-ferrite content in 304L (~2–3%). The Hall–Petch consistency check indicates that grain size played a minor, and negligible role in the observed strength evolution. The observed differences in measured strength are qualitatively consistent with literature-reported heat-treatment-related defect-structure evolution, including possible solute redistribution and stabilization of dislocation substructures.

Overall, the proposed workflow improves qualification traceability by combining destructive mechanical-property measurement, microstructural characterization, and ECT-based near-surface defect screening on the same material heats. The approach is practically useful for industrial acceptance screening, but it is not presented as a quantitative NDT method for predicting mechanical properties or as a full POD-qualified inspection procedure.

Author Contributions: Conceptualization, J.E.; methodology, J.E. and A.S.; software, J.E.; validation, M.N.R. and J.D.; formal analysis, J.E.; investigation, S.B. and J.E.; resources, S.B. and A.S.; data curation, J.E.; writing—original draft preparation, J.E. and M.N.R.; writing—review and editing, A.S., S.B. and J.D.; visualization, J.E.; supervision, A.S.; project administration, J.E.; funding acquisition, A.S. All authors have read and agreed to the published version of the manuscript.

Funding: This research was financially supported by the European Union under the REFRESH—Research Excellence For Region Sustainability and High-tech Industries project (No. CZ.10.03.01/00/22_003/0000048) via the Operational Programme Just Transition. It was also supported by the project Students Grant Competition SP2026/070 titled "Research, Development, and Innovation in the Field of Transport and Logistics 2025," financed by the Ministry of Education, Youth and Sports and the Faculty of Mechanical Engineering.

Institutional Review Board Statement: Not applicable.

Informed Consent Statement: Not applicable.

Data Availability Statement: The data presented in this paper can be made available on request from the corresponding author.

Acknowledgments: All authors have read and agreed to the published version of the manuscript. The authors would like to thank the Faculty of Mechanical Engineering of Vysoka skola banska-Technical University of Ostrava (VSB-TUO) for their support.

Conflicts of Interest: The authors declare no conflicts of interest.

Abbreviations

List of key acronyms used in the manuscript:

A	Percentage elongation to failure (%)
AISI	American Iron and Steel Institute
ANSYS FEA/FEM	Finite Element Analysis/Finite Element Method
ASTM	American Society for Testing and Materials
BCC	Body-Centered Cubic
Charpy KV	Charpy V-notch absorbed impact energy (J)
DBT/DBTT	Ductile-to-Brittle Transition/Ductile-to-Brittle Transition Temperature
DT	Destructive Testing
ECT (EC)	Eddy Current Testing (Eddy Current)
FCC	Face-Centered Cubic
LOM	Light Optical Microscopy
NDT	Non-Destructive Testing
POD	Probability of Detection
SEM	Scanning Electron Microscopy
σ_γ (Rp0.2)	0.2% Offset Yield Strength (MPa)
UTS/σUTS	Ultimate Tensile Strength (MPa)
μ	Mean value (noise baseline)
σ	Standard deviation
δ-ferrite	Delta ferrite phase in austenitic stainless steels
ΔZ	Change in probe impedance (ECT signal)
Z_0	Baseline impedance (ECT reference signal)

References

1. Desu, R.K.; Krishnamurthy, H.N.; Balu, A.; Gupta, A.K.; Singh, S.K. Mechanical properties of Austenitic Stainless Steel 304L and 316L at elevated temperatures. *J. Mater. Res. Technol.* **2016**, *5*, 13–20. [CrossRef]
2. Ragheb, T.; Geddes, L.A. Electrical properties of metallic electrodes. *Med. Biol. Eng. Comput.* **1990**, *28*, 182–186. [CrossRef] [PubMed]
3. Shen, X.; Lu, X.; Guo, J.; Liu, Y.; Qi, J.; Lv, Z. Nondestructive Testing of Metal Cracks: Contemporary Methods and Emerging Challenges. *Crystals* **2023**, *14*, 54. [CrossRef]
4. Emele, J.; Sliva, A.; Ramasamy, M.N.; Fusek, M.; Besta, P.; Dižo, J. Reviewing Critical Logistics and Transport Models in Stainless-Steel Fluid Storage Tanks. *Eng* **2025**, *6*, 275. [CrossRef]
5. Rao, M.N. Materials Development for Indian Nuclear Power Programme: An Industry Perspective. *Energy Procedia* **2011**, *7*, 199–204. [CrossRef]

6. Navon, R.; Berkovich, O. An automated model for materials management and control. *Constr. Manag. Econ.* **2006**, *24*, 635–646. [CrossRef]
7. Frank, J.F.; Chmielewski, R. Influence of Surface Finish on the Cleanability of Stainless Steel. *J. Food Prot.* **2001**, *64*, 1178–1182. [CrossRef]
8. Kelidari, Y.; Kashefi, M.; Mirjalili, M.; Seyedi, M.; Krause, T.W. Eddy current technique as a nondestructive method for evaluating the degree of sensitization of 304 stainless steel. *Corros. Sci.* **2020**, *173*, 108742. [CrossRef]
9. Sgobba, S.; Santillana, I.A.; Ruiz-Palenzuela, B.; Castro, E.R.; Knaster, J.; Schild, T.; Han, S.; Rossano, G.; Libeyre, P.; Beemsterboer, C. Lessons learnt from manufacturing—Forging of tokamak components. *Fusion Eng. Des.* **2025**, *212*, 114869. [CrossRef]
10. Favre, A.; Valente, R.; Olivero, D.; Baisotti, M.; Viotto, L. A Study of Void Closure in Hot Rolling Bars of Stainless Steel. In *Proceedings of the 14th International Conference on the Technology of Plasticity—Current Trends in the Technology of Plasticity, ICTP 2023, Lecture Notes in Mechanical Engineering*; Springer: Cham, Switzerland, 2024; pp. 275–282. [CrossRef]
11. Stashkov, A.N.; Nichipuruk, A.P.; Schapova, E.A.; Gordeev, N.V.; Vshivtsev, I.V.; Kazantseva, N.V. Magnetic Properties of Cyclically Tensile-Deformed Steel 09G2S Manufactured by Selective Laser Melting. *Russ. J. Nondestruct. Test.* **2023**, *59*, 54–61. [CrossRef]
12. Krapez, J.-C. Thermal effusivity profile characterization from pulse photothermal data. *J. Appl. Phys.* **2000**, *87*, 4514–4524. [CrossRef]
13. Dell'aVvocato, G.; Cusanno, A.; Bison, P.; Rossi, S.; Palumbo, G.; Ferrarini, G. Non-destructive assessment of crystallographic texture and mechanical behaviour in AZ31 magnesium alloys via pulsed laser thermography. *Quant. Infrared Thermogr. J.* **2026**, *23*, 53–67. [CrossRef]
14. Nicolaides, L.; Mandelis, A.; Beingessner, C.J. Physical mechanisms of thermal-diffusivity depth-profile generation in a hardened low-alloy Mn, Si, Cr, Mo steel reconstructed by photothermal radiometry. *J. Appl. Phys.* **2001**, *89*, 7879–7884. [CrossRef]
15. van der Veen, A.; Nater, D. Sample preparation from bulk samples: An overview. *Fuel Process. Technol.* **1993**, *36*, 1–7. [CrossRef]
16. *ASTM International AA 24a*; Standard Test Methods and Definitions for Mechanical Testing of Steel Products. ASTM International: West Conshohocken, PA, USA, 2024.
17. Deng, Y.; Yang, M.; Lei, L.; Zhao, F.; Wang, P.; Long, S.; Xu, F. Synergistic engineering of strength, ductility, and corrosion resistance in 316 austenitic stainless steel via cryogenic rolling and tailored annealing. *Mater. Charact.* **2025**, *228*, 115395. [CrossRef]
18. Che, P.; Xie, L.; Sultana, S.; Wang, N.; Yang, L.; Zhao, W.; Ning, Z.; Sun, J.; Wang, S.; Huang, Y. Microstructure evolution and failure mechanism of SP2215/Stellite-6 components prepared by laser directed energy deposition during high-temperature service. *Mater. Charact.* **2026**, *233*, 116112. [CrossRef]
19. Kalpakjian, S. Mechanical Testing for Metalworking Processes. In *Mechanical Testing and Evaluation*; ASM International: West Conshohocken, PA, USA, 2000; pp. 70–78. [CrossRef]
20. Jordan, E.C.; Andrews, C.L. Electromagnetic Waves and Radiating Systems. *Am. J. Phys.* **1951**, *19*, 477–478. [CrossRef]
21. Dolati, S.S.K.; Caluk, N.; Mehrabi, A.; Dolati, S.S.K. Non-Destructive Testing Applications for Steel Bridges. *Appl. Sci.* **2021**, *11*, 9757. [CrossRef]
22. Scheirer, N.D.; Holland, S.D. Model-Quality-Adaptive Probability of Detection Across Multiple Inspection Scenarios. *J. Nondestruct. Eval.* **2025**, *44*, 154. [CrossRef]
23. He, K.; Chen, Y.; Lai, H.; Wu, X. Mechanical response and constitutive model of austenitic 304 stainless steel after exposure ISO 834 fire. *J. Constr. Steel Res.* **2025**, *224*, 109144. [CrossRef]
24. Rasmussen, K.J. Full-range stress–strain curves for stainless steel alloys. *J. Constr. Steel Res.* **2003**, *59*, 47–61. [CrossRef]
25. Lee, I.; Merickel, J.W.; Sreenivasulu, Y.K.; Xu, F.; Tang, Y.; Rittenhouse, J.E.; Vakanski, A.; Song, R. Comprehensive Toughness Dataset of Nuclear Reactor Structural Materials using Charpy V-Notch Impact Testing. *Sci. Data* **2025**, *12*, 543. [CrossRef]
26. Kazakeviciute, J.; Rouse, J.P.; Focatiis, D.; Hyde, C. Small specimen techniques for estimation of tensile, fatigue, fracture and crack propagation material model parameters. *J. Strain Anal. Eng. Des.* **2022**, *57*, 227–254. [CrossRef]
27. Zhang, Y.-H.; Ma, E.; Sun, J.; Han, W.-Z. A unified model for ductile-to-brittle transition in body-centered cubic metals. *J. Mater. Sci. Technol.* **2023**, *141*, 193–198. [CrossRef]
28. Hwang, B.; Lee, T.-H.; Kim, S.-J. Effects of deformation-induced martensite and grain size on ductile-to-brittle transition behavior of austenitic 18Cr-10Mn-N stainless steels. *Met. Mater. Int.* **2010**, *16*, 905–911. [CrossRef]
29. Riganti, G.; Cadoni, E. Ductile-to-Brittle Transition of Steel Due to Dynamic Loading. *Metals* **2024**, *14*, 807. [CrossRef]
30. Aydemir, B. Uncertainty Analysis in the Notch Impact Test, for Materials with Different Energy Levels. *Acta Polytech. Hung.* **2021**, *18*, 187–200. [CrossRef]
31. Gangwar, V.; Acharyya, S.; Banerjee, A. Calibration of tensile tests in drop-weight impact machine and implementation in simulation of Charpy impact tests. *Procedia Struct. Integr.* **2024**, *60*, 123–135. [CrossRef]
32. Rodrigues, P.F.; Teixeira, R.S.; Le Sénéchal, N.V.; Fernandes, F.M.B.; Paula, A.S. The Influence of the Soaking Temperature Rotary Forging and Solution Heat Treatment on the Structural and Mechanical Behavior in Ni-Rich NiTi Alloy. *Materials* **2021**, *15*, 63. [CrossRef]

33. Arata, Y.; Matsuda, F.; Katayama, S. Solidification crack susceptibility in weld metals of fully austenitic stainless steels (Report II): Effect of ferrite, P, S, C, Si and Mn on ductility properties of solidification brittleness. *Trans. JWRI* **1977**, *6*, 105–116.
34. Dunstan, D.; Bushby, A. Grain size dependence of the strength of metals: The Hall–Petch effect does not scale as the inverse square root of grain size. *Int. J. Plast.* **2014**, *53*, 56–65. [CrossRef]
35. Farag, H.E.; Khamesee, M.B.; Toyserkani, E. Eddy Current Sensor Probe Design for Subsurface Defect Detection in Additive Manufacturing. *Sensors* **2024**, *24*, 5355. [CrossRef]
36. Saddoud, R.; Perlin, K.; Sergeeva-Chollet, N.; Delacroix, T.; Skarlatos, A.; Garandet, J. On the potential of eddy current characterization of the ferritic content of recovered 316L powders after LaserPowder bed fusion fabrication. *Addit. Manuf. Lett.* **2024**, *9*, 100207. [CrossRef]
37. Du, L.-Y.; Lu, H.-H.; Xing, Z.-Z.; Wang, Y.-N.; Han, J.-S.; Zou, Y. Effects of σ phase embrittlement and Al addition on the ductile-brittle transition in super ferritic stainless steels. *Mater. Sci. Eng. A* **2025**, *920*, 147564. [CrossRef]
38. Xing, Z.-Z.; Lu, H.-H.; Han, J.-S.; Yang, B.; Wang, Y.-N.; Du, L.-Y. Tailoring the brittle phase precipitation and mechanical properties in developing ultra-super ferritic stainless steels by Al modification. *Mater. Des.* **2023**, *236*, 112519. [CrossRef]
39. Fadeeva, G.; Maksymov, S.; Jia, C.; Vasiliev, D.; Radzievska, A. Determination of the quantitative phase composition of the metal of welded joints of high-alloy steels, including duplex steels. *Paton Weld. J.* **2025**, *2025*, 3–12. [CrossRef]
40. Maehara, Y.; Ohmori, Y.; Kunitake, T. Effect of σ-phase precipitation on hot ductility in δ-ferrite-austenite duplex stainless steels. *Met. Technol.* **1983**, *10*, 296–303. [CrossRef]